Radiology

PET/MR Imaging: Technical Aspects and Potential Clinical Applications[1]

Drew A. Torigian, MD, MA
Habib Zaidi, PhD
Thomas C. Kwee, MD, PhD
Babak Saboury, MD, MPH
Jayaram K. Udupa, PhD
Zang-Hee Cho, PhD
Abass Alavi, MD

Instruments that combine positron emission tomography (PET) and magnetic resonance (MR) imaging have recently been assembled for use in humans, and may have diagnostic performance superior to that of PET/computed tomography (CT) for particular clinical and research applications. MR imaging has major strengths compared with CT, including superior soft-tissue contrast resolution, multiplanar image acquisition, and functional imaging capability through specialized techniques such as diffusion-tensor imaging, diffusion-weighted (DW) imaging, functional MR imaging, MR elastography, MR spectroscopy, perfusion-weighted imaging, MR imaging with very short echo times, and the availability of some targeted MR imaging contrast agents. Furthermore, the lack of ionizing radiation from MR imaging is highly appealing, particularly when pediatric, young adult, or pregnant patients are to be imaged, and the safety profile of MR imaging contrast agents compares very favorably with iodinated CT contrast agents. MR imaging also can be used to guide PET image reconstruction, partial volume correction, and motion compensation for more accurate disease quantification and can improve anatomic localization of sites of radiotracer uptake, improve diagnostic performance, and provide for comprehensive regional and global structural, functional, and molecular assessment of various clinical disorders. In this review, we discuss the historical development, software-based registration, instrumentation and design, quantification issues, potential clinical applications, potential clinical roles of image segmentation and global disease assessment, and challenges related to PET/MR imaging.

Supplemental material: *http://radiology.rsna.org/lookup/suppl/doi:10.1148/radiol.13121038/-/DC1*

[1] From the Department of Radiology, Hospital of the University of Pennsylvania, 3400 Spruce St, Philadelphia, PA 19104-4283 (D.A.T., B.S., J.K.U., A.A.); Division of Nuclear Medicine and Molecular Imaging, Geneva University Hospital, Geneva, Switzerland (H.Z.); Geneva Neuroscience Center, Geneva University, Geneva, Switzerland (H.Z.); Department of Nuclear Medicine and Molecular Imaging, University Medical Center Groningen, University of Groningen, Groningen, the Netherlands (H.Z.); Department of Radiology, University Medical Center Utrecht, Utrecht, the Netherlands (T.C.K.); and Neuroscience Research Institute, Gachon University of Medicine and Science, Incheon, South Korea (Z.H.C.). Received June 8, 2012; revision requested July 27; revision received December 8; accepted December 27; final version accepted December 28. Supported by the Swiss National Science Foundation under grants SNSF 31003A-135576, 33CM30-124114, Geneva Cancer League, and the Indo-Swiss Joint Research Programme ISJRP 138866. **Address correspondence to** D.A.T. (e-mail: *Drew.Torigian@uphs.upenn.edu*).

Several investigators have proposed or developed techniques to improve the correlation between molecular and structural information from positron emission tomography (PET) and magnetic resonance (MR) imaging. This includes software-based image registration, in which different studies are fused after acquisition with individual imaging systems. Image registration techniques commonly produce a single fused or combined image, with the PET image displayed in color over a gray-scale MR image of the same anatomic region (1,2).

Software image fusion can be challenging in the clinical setting because it requires exceptional Digital Imaging and Communications in Medicine connectivity and compatibility among imaging protocols and modalities. These challenges may be overcome by the concurrent use of PET and MR imaging systems, although software-based registration offers greater flexibility and may sometimes offer complementary advantages to hardware-based approaches (3,4).

Achieving a high degree of accuracy for spatial transformation between image sets can be quite complicated. Physical factors such as noise, limited spatial resolution, attenuation, scatter, and partial volume effect and biologic factors such as persistent activity in the blood pool and nonspecific radiotracer uptake may decrease contrast and create blurring on images, making the landmark localization required for coregistration difficult. The registration problem for imaging of the brain is quite different from that in whole-body imaging. Furthermore, diagnostic MR images are usually obtained during breath hold, whereas PET data are acquired during longer time periods so that the resultant reconstructed image set is an average of all phases of respiration (5). Thus, PET/MR imaging of the thorax, abdomen, or pelvis, where organ motion exists, may result in inconsistent image sets. This inconsistency can cause problems; for example, if the body boundaries on MR and PET images can be registered but the internal structures differ substantially. Various short dual-modality imaging protocols that use a common respiratory pattern have been designed to avoid the breath-holding problem (6). In these protocols, the MR imaging data allow for registration with corresponding PET images for accurate localization of metabolic abnormalities. Despite the difficulties, many semiautomated or fully automated registration methods have been developed and used with various degrees of success for both research and clinical purposes (7). An in-depth overview of software-based registration techniques and algorithms is beyond the scope of this review, although recent comprehensive reviews are available for interested readers (6,8–10).

Two main strategies have emerged for performing rigid registration such as PET/MR imaging registration of brain images from the same patient. The first strategy is to identify similar structures on both images and subsequently minimize a distance measurement between them. The second strategy is voxel-to-voxel measurement of the full three-dimensional set of data as the matching criterion. The criterion used in the registration algorithm is known as the similarity measure, and the most popular criteria include minimization of histographic dispersion (11), maximization of mutual information (12), or maximization of the correlation ratio (13). Mutual information, the most widely used, is an intensity-based similarity measure, and many variants to this approach have been proposed.

Nonrigid registration approaches are usually required to correlate images of the thorax and abdomen and are often used in combination with linear registration techniques to correct for changes in body configuration, differences in breathing patterns, or internal organ motion and associated displacement. For response assessment where intrapatient registration of pre- and posttreatment whole-body PET images may be required to automate lesion analysis (14,15), nonrigid registration with position-dependent rigidity approaches has been suggested. These techniques assign a high degree of rigidity to some regions (eg, lesions and brain) that will remain unchanged after the registration process (16).

Essentials

- PET/MR imaging may be performed either by using software-based registration of independently acquired PET and MR image data sets, or by using sequential or concurrent PET/MR imaging instrumentation.
- PET/MR imaging offers the potential for robust combined structural, functional, and molecular imaging assessment of a wide variety of oncologic, neurologic, cardiovascular, and musculoskeletal conditions; further research will be required to demonstrate the incremental benefit of PET/MR imaging compared with PET/CT imaging in various clinical and research settings.
- Challenges beyond those of a technical nature remain for PET/MR imaging, including the need for comparative effectiveness and additional safety assessments as well as standardization of appropriateness criteria, image acquisition parameters, radiotracer and contrast material–injection protocols, personnel qualifications, and reimbursement guidelines.

Instrumentation and Design of PET/MR Imaging

The excellent soft-tissue contrast of MR images and the advanced functional MR imaging options available complement

Published online
10.1148/radiol.13121038 **Content codes:** MR MI

Radiology 2013; 267:26–44

Abbreviations:
ADC = apparent diffusion coefficient
DW = diffusion weighted
FDG = ^{18}F-2-fluorodeoxyglucose
Gd-EOB-DTPA = gadolinium-ethoxybenzyl-diethylenetriamine pentaacetic acid
SUV = standardized uptake value

Conflicts of interest are listed at the end of this article.

Figure 1

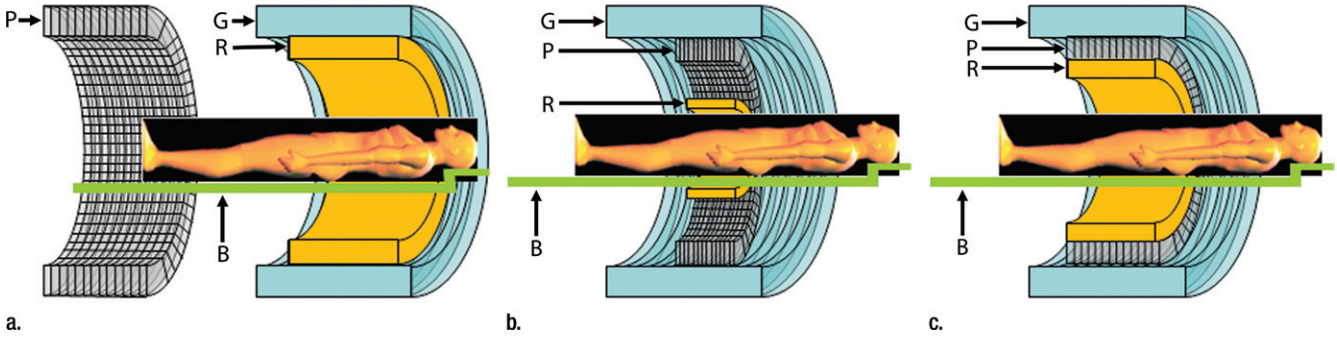

Figure 1: Schematic cross-sectional views of potential designs for combined PET/MR imaging systems: **(a)** tandem design with two imagers mounted back-to-back (similar to that in PET/CT instrumentation) to allow sequential rather than simultaneous acquisition, **(b)** insert design with PET imager *(P)* inserted between radiofrequency coil *(R)* and gradient set *(G)* of MR imager, and **(c)** fully integrated design with two imagers in same gantry. Radiofrequency coil, gradient set, PET imager, and patient bed *(B)* are shown for all configurations.

the molecular information PET provides. The development of a fully integrated PET/MR imaging system is technologically challenging and requires not only substantial modifications of the PET subsystem to make it compact and insensitive to strong magnetic fields but also a major redesign of MR imaging hardware.

Sequential

The most straightforward approach for PET/MR imaging is the serial arrangement, in which both modalities are used sequentially end-to-end on two distinct systems as part of a single examination (Fig 1a). Two design concepts have emerged depending on whether both imaging systems are located in the same room or in two separate rooms. The former was implemented by Philips Healthcare (Best, the Netherlands) (17), and the latter was implemented by GE Health Care (Milwaukee, Wis) (18). The same patient-transfer tabletop is docked on both imaging gantries and used for both PET/CT and MR imaging examinations. This approach is economical because relatively minor modifications are required to shield the PET subsystem from the magnetic field and to arrange for patient bed transfer from one imaging unit to the other (19). Moreover, the image quality and quantification each system provides are virtually unchanged by the assembly. However, the serial rather than parallel data acquisition is an important limitation that may render the system more susceptible to motion artifacts and prevents simultaneous PET and MR imaging data acquisition, which may be important for certain clinical and research applications. Also, a large room is needed compared with that required for PET/CT or concurrent PET/MR imaging. For example, the typical room size needed for the Ingenuity TF PET/MR imaging system (Philips Healthcare) is approximately 4.3 × 13 m, which may be challenging to secure (Fig 2a).

GE Healthcare proposed an alternative that enables trimodality imaging (PET, CT, and MR imaging) and uses sequential acquisition on two separate imagers (PET/CT and MR imaging) in adjacent rooms. The patient is shuttled from one imager to the other by means of a mobile bed (18). The advantage of this solution is that the two imaging units can be operated separately in cases of high workload. A major drawback and logistical challenge is the coordination of patient transfer between imagers, which presents a higher risk of patient motion. This design also requires performance of a CT scan for attenuation correction of the PET data, which increases the radiation dose to the patient.

The spatial resolution in PET depends on the design of the PET subsystem, and as such, this parameter is not expected to vary when PET is combined with another imaging modality. The spatial resolution has been reported to be comparable in the Ingenuity TF PET/MR imaging and Gemini TF PET/CT systems (Philips Healthcare), demonstrating the effectiveness of magnetic shielding and overall system design, which resulted in proper photomultiplier tube calibration and operation (17).

Concurrent

The combination of two imaging modalities in a single gantry entails rigorous technical issues that must be addressed. The development of an MR imaging–compatible PET imager must address two major restrictions: space restrictions inside the MR imaging magnet and interference between the two imaging modalities. Photodetector technologies that are not sensitive to magnetic fields and readout electronics with minimal heat radiation are required (20). The operation of the MR imaging unit should not be affected by the PET detector components owing to electronic interference on the radiofrequency and gradient coils. This is more problematic if the readout electronics use high frequency digital clocks or if eddy currents are generated (21,22). Moreover, the performance of both subsystems should remain similar to what can be achieved on modern, independent imagers. Delso et al (23) recently reported that the interference between PET and

Figure 2

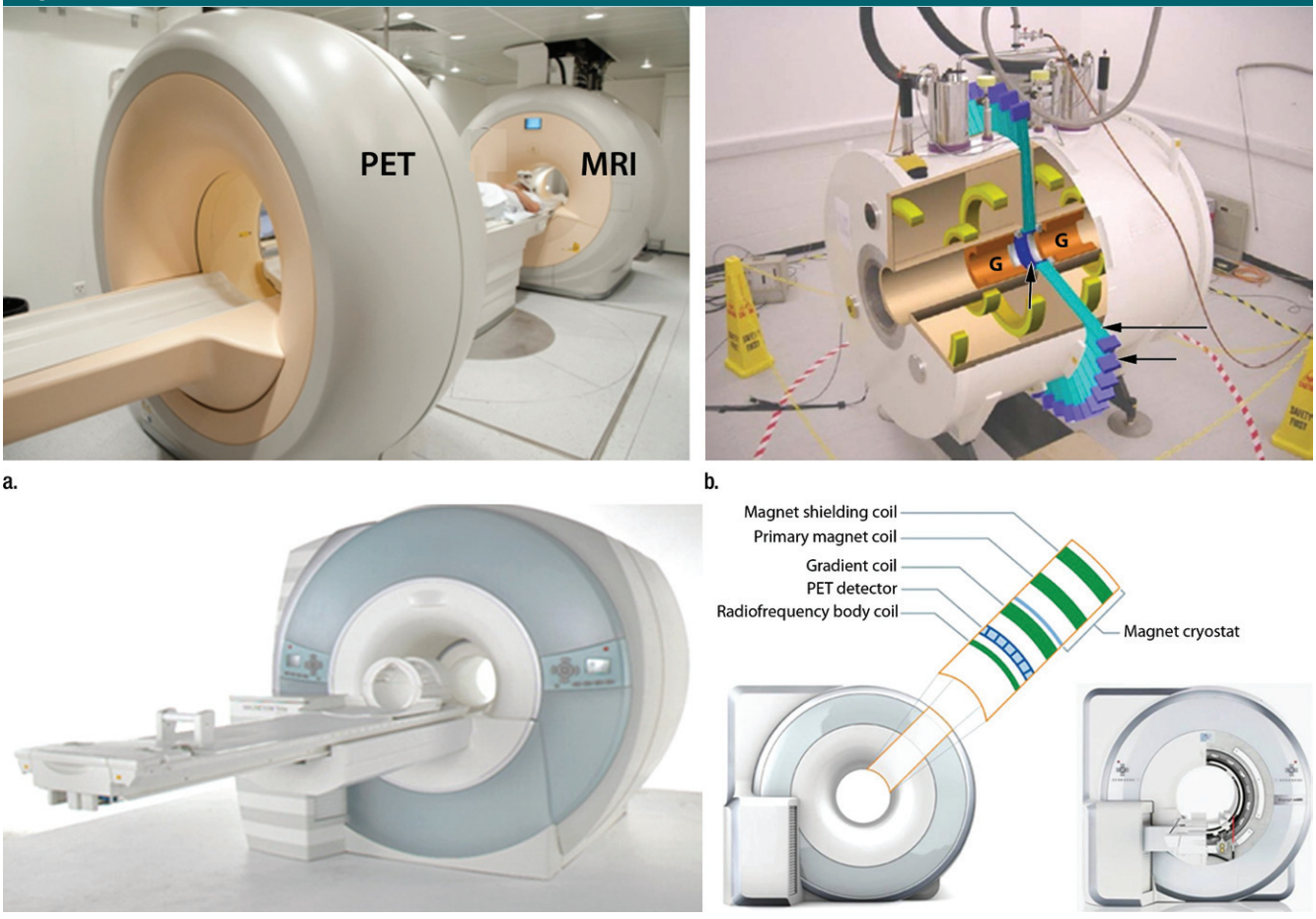

Figure 2: Representative PET/MR imaging instruments. **(a)** Photograph of whole-body Ingenuity TF PET/MR imaging system (Philips Healthcare) installed at Geneva University Hospital, Switzerland. Turntable system facilitates patient motion between Achieva X series 3-T MR imaging system on right and time-of-flight PET system on left. **(b)** Cutaway schematic of split-magnet of PET/MR imaging shows scintillation crystal ring (vertical arrow), fiber bundles (horizontal long arrow), screened photomultiplier tubes outside magnet cryostat (horizontal short arrow), and split gradient coil *(G)*. (Modified and reprinted, with permission, from reference 28.) **(c)** Photograph of integrated BrainPET PET/MR imaging design (Siemens Healthcare) consists of isocentric layering of MR imaging head coil, PET detector ring, and MR imaging magnet tunnel. **(d)** Schematic view of whole-body Biograph mMR PET/MR imaging prototype showing basic system components in which PET detector ring is placed between radiofrequency coil and gradient coil. (Image courtesy of Siemens Healthcare.)

MR imaging is almost insignificant with the Biograph mMR hybrid imager (Siemens Healthcare, Erlangen, Germany).

The initial remedy implemented in the pioneering work by Christensen et al (24) to reduce interference consisted of positioning crystals inside the MR imaging system and placing conventional photomultiplier tubes up to 5 m away from the crystals. The photomultiplier tubes were later replaced by position-sensitive avalanche photodiodes (25), although the requirement to convey scintillation light beyond the magnetic field restricts the PET axial field of view. Loss of scintillation light also occurs, which degrades the energy resolution of PET detectors.

Subsequently, three design concepts emerged for concurrent PET/MR imaging systems: PET insert (Fig 1b), fully integrated PET/MR imaging (Fig 1c), and the split-field magnet (Fig 2b) (20,26). An analogous photomultiplier tube–based design with a split-magnet low-field-strength MR imaging system and a large number of PET detectors in the MR imaging unit gap also exists, with decreased fiber length (26). The system is based on the microPET Focus 120 preclinical system (Siemens Molecular Imaging Preclinical Solutions, Knoxville, Tenn) (27), and is housed in a split region of a 1-T actively-shielded superconducting magnet. The scintillation light is conveyed to the photomultiplier tubes by using 1.2-m-long fiber, which results in a negligible effect on image quality. Various investigators have assessed the effect of long fibers on PET subsystem performance and have reported degradation of many PET

subsystem performance parameters including sensitivity and energy, timing, and spatial resolution (24,28). Authors of another study (26) reported on comparative assessment of long (1.2 m) and short (0.1 m) fibers demonstrating minor sensitivity loss but substantial degradation of energy resolution at the photopeak (17.2%–27.1%), with approximately 40% light loss for long fibers, and time resolution (2.6–3.6 nsec). More importantly, despite deterioration of the position map on the photomultiplier tubes, spatial resolution remained almost unchanged (approximately 1.6 mm) (26). The main disadvantage of this design is that it entails a nonconventional lower field magnet, but the main advantage is excellent decoupling of electronic crosstalk between PET and MR imaging.

Another design concept takes advantage of recent developments in the field of solid-state detectors, such as avalanche photodiodes, to build a PET detector insert that is not sensitive to the magnetic field, and therefore, can be placed inside a standard MR imaging unit. The outlook for this setup has been described (25,29–43) in research that is focused on small animal imaging (44). The first simultaneously acquired PET/MR images relied on use of an avalanche photodiode–based PET insert placed in a small-animal MR imaging unit (25). Usually, PET inserts use detector rings with smaller diameters (approximately 6 cm) so that they fit into the MR imaging unit without impeding space occupied by conventional MR imaging gradients. For instance, the standard gradient set for a 200-mm bore magnet reduces clear bore access from 200 to 120 mm (20).

The PET subsystem of modules of the most recent design of preclinical PET/MRI development subsequent to significant improvements of the original design consist of 10 cerium-doped lutetium oxyorthosilicate avalanche photodiode detector modules with axial and transaxial fields of view of 19 mm and 40 mm, respectively (33). The detector modules comprise a 12 × 12 cerium-doped lutetium oxyorthosilicate scintillator array (1.6 × 1.6 × 4.5 mm^3), a 3 × 3 avalanche photodiode array, and custom charge-sensitive preamplifier electronics placed inside a thin copper-shielded housing (36,37). A similar design was adopted for the BrainPET hybrid system (Fig 2c) (42). Despite challenges associated with this design in terms of instability in daily operation, authors of ongoing studies on both preclinical and brain imager prototypes have provided preliminary evidence about its feasibility in the research setting. However, the concept is still far from application as a commercial product. Another concern is the relatively poor timing resolution of avalanche photodiode–based detector modules, which prevents implementation of time-of-flight technology (45). Also, interference of the MR imaging unit with PET electronics degrades PET performance (44). A slight increase in magnet radius substantially increases its cost, and an increase of inner diameter of the gradient considerably reduces strength and efficiency of gradient sets. Currently available commercial preclinical MR imaging units can accommodate the combined gradient set and PET imager assembly without increasing magnet cost.

The most promising concept for PET/MR imaging is a fully integrated compact system combining PET and MR imaging units in a single device. Introduction of PET detector electronic components into the gradient and radiofrequency coils of the MR imaging unit might affect MR imaging signal-to-noise ratio (44). Nevertheless, those electronic components will not have an unavoidable effect on the MR imaging system owing to the relatively narrow MR imaging operating frequency band. Furthermore, use of walled screens (0.15-mm copper) to offer suitable electromagnetic attenuation to avoid interference with PET electronics may be useful, although this can decrease signal-to-noise ratio by approximately 30% (33). Optimal system performance might be compromised and will be difficult to reach and sustain unless the shims, gradients, and radiofrequency transmitter are integrated (20).

The Biograph mMR whole-body PET/MR imaging prototype is one example of an integrated compact hybrid system (Fig 2d). The system has been assessed in clinical facilities (23,46). The PET imager has eight rings of 56 detector blocks for a ring diameter of 65.6 cm and an axial field of view of 25.8 cm, and each PET detector block comprises 8 × 8 cerium-doped lutetium oxyorthosilicate crystals read out by a matrix of 3 × 3 avalanche photodiodes. The transaxial and axial fields of view of the MR imaging subsystem are 50 and 45 cm, respectively. The MR imaging subsystem was specifically designed for the Biograph mMR and is fully integrated with the architecture of the PET subsystem (20).

Hybrid PET/MR imaging technology will benefit from the latest designs in front-end electronics and dedicated high-performance asynchronous specific integrated circuits. The advent of multicell Geiger-mode avalanche photodiodes (also known as silicon photomultiplier tubes) for light detection will be important in future design of integrated PET/MR imaging systems to achieve minimal interference between PET and MR imaging. There has been rapid growth in the use of silicon photomultiplier tubes, and they have achieved the level of performance required for the design of advanced medical imaging systems because they are small, light, and insensitive to magnetic fields (47–52).

Compared with other solid-state photodetectors such as avalanche photodiodes, silicon photomultiplier tubes have much-improved characteristics in terms of gain, signal-to-noise ratio, and timing resolution, which make them good candidates for time-of-flight PET (53) and time-of-flight PET/MR imaging systems. Preliminary results obtained by using silicon photomultiplier tubes inside a magnetic field while running MR imaging gradients and radiofrequency pulses indicate that their performance is not affected by the static magnetic field or gradient switching (54).

The conventional silicon photomultiplier tube is, in essence, an analog device whose linearity is governed by its intrinsic granularity and number of microcells. The current trend in modern

PET instrumentation is to move toward fully digital readout technology and handling of data and signals (45). It is therefore desirable to have digital solid-state detectors to circumvent the requirement for dedicated components such as amplifiers, asynchronous specific integrated circuits, and analog-to-digital converters. The proof of principle was recently demonstrated by using digital silicon photomultiplier tubes derived from single avalanche photodiodes incorporated in a typical complementary metal-oxide semiconductor process (55,56). The field is still in its infancy and more promising developments in complementary metal-oxide semiconductor technology that will have an enormous effect on future designs of PET/MR imaging systems are anticipated (20).

The instrumentation requirements for future generation MR imaging–compatible PET detector modules are extremely challenging given the number and level of complexity of technical issues that must be addressed. PET detectors should be capable of providing highly accurate three-dimensional spatial information and fast-timing information in addition to a high intrinsic efficiency. The matrices of pixilated crystals or continuous crystals combined with fast and highly granular photodetectors could serve as the basis for PET detector module design.

Many different design paths are being pursued, some commercially available and ready for clinical use, but they are limited to use in academic facilities with advanced technical and scientific support. Although it is not clear which ones will be preferred in future commercial systems, it is certain that technologic advances will continue and will enable novel clinical applications of multimodality and multiparametric imaging. Furthermore, more research is needed to compare concurrent PET/MR imaging with sequential PET/MR imaging in clinical use for differences in cost effectiveness.

Please see Appendix E1 (online) for details regarding the historical development of and quantification issues related to PET/MR imaging.

Potential Clinical Applications of PET/MR Imaging

An overview of the key issues regarding cost and workflow of integrated imaging systems versus standalone imaging devices is discussed in detail elsewhere (57,58). Manufacturers currently offer different options for operation of hybrid PET/MR imaging units in the clinical setting. Usually, a single, short MR imaging sequence is used for both anatomic referencing and attenuation correction of PET data (17,57), which leaves time for acquisition of additional MR imaging sequences required for the study. MR imaging–guided motion correction in PET is rarely applied in the clinical setting but usually necessitates additional concurrently acquired MR images in research investigations (eg, a tagged MR imaging sequence that can impose a spatially periodic magnetization pattern of linear tags on a tissue of interest that moves with the tissue and undergoes motion distortion, allowing for quantitative measurement of tissue motion) (59). In general, image acquisition times for concurrent and sequential PET/MR imaging systems in patients with oncologic disease may range from about 30 to 70 minutes and 40 to 90 minutes, respectively, depending on the specific clinical question to be addressed, the anatomic region of coverage (partial vs whole body), and the number and types of MR imaging sequences to be obtained in each anatomic region. However, image acquisition times are generally lower in patients with neurologic, cardiovascular, and musculoskeletal disease if the anatomic regions of coverage are more limited.

Oncologic Disease

MR imaging provides useful structural and functional information about malignancy that is complementary to the information provided by PET (60,61–66). MR imaging provides high spatial resolution definition of tumor volume and local disease extent for tumor staging because of its superior soft-tissue contrast and is particularly useful for the evaluation of primary tumors that originate from anatomic sites that are suboptimally evaluated at CT (ie, the brain, head and neck, spinal cord, liver, pelvic organs, breasts, and musculoskeletal system). Fluorine 18 (^{18}F)-2-fluoro-2-deoxy-D-glucose (FDG) PET, in general, provides improved molecular detection and characterization of lymph nodes as benign or malignant for node staging (62,67–69). Reports of the potential clinical applications of PET/MR imaging for local-regional assessment of cancer are as follows.

Boss et al (70) prospectively studied eight patients with head and neck tumors by using simultaneous FDG PET/MR imaging after FDG PET/CT. MR imaging datasets showed excellent image quality without recognizable artifacts caused by the inserted PET system, and PET images from PET/MR imaging exhibited better spatial resolution and image contrast compared with those from PET/CT. Furthermore, excellent agreement between metabolic ratios (defined as radiotracer uptake in normal anatomic structures or tumor related to the cerebellum) from both PET systems was found with correlation coefficients of 0.99 and 0.96 for normal anatomic structures and tumors, respectively.

Huang et al (71) compared software-registered FDG PET/MR imaging with FDG PET/CT, MR imaging, and CT to assess surrounding tissue invasion in 17 patients with advanced buccal squamous cell carcinoma and suspected masticator space invasion on the basis of CT imaging. The likelihood ratio was highest for FDG PET/MR imaging (42.56) compared with FDG PET/CT (25.02), MR imaging (22.94), and CT (8.6; all $P < .05$), because PET/MR imaging was superior for demonstrating tumor involvement in both local bone and muscle regions (and especially for revealing masseter muscle invasion). The sensitivity and specificity of PET/MR imaging were also highest among the four modalities (90% [18 of 20]/91% [40 of 44], 80% [16 of 20]/84% [37 of 44], 80% [16 of 20]/80% [35 of 44], and 55% [11 of 20]/82% [36 of 44], for FDG PET/MR, FDG PET/CT, MR, and CT, respectively). The level of diagnostic confidence was higher for fused FDG PET/MR imaging or MR imaging than

FDG PET/CT or CT (85.9%, 85.9%, 70.3%, and 73.4%, respectively). Huang et al (71) concluded that FDG PET/MR imaging is more reliable for focal invasion assessment and tumor size delineation in advanced buccal squamous cell carcinoma compared with FDG PET/CT, MR imaging, and CT.

Nagarajah et al (72) prospectively compared Iodine 124 PET/CT and software-registered Iodine 124 PET/MR imaging for diagnosis and dosimetry of thyroid remnant tissues and lymph node metastases in 33 patients with high-risk differentiated thyroid carcinoma who had undergone thyroidectomy and had received Iodine 124 PET/CT dosimetry before radioiodine therapy and contrast material–enhanced MR imaging of the neck. Analyses of lesions at PET (n = 106 Iodine 124 PET positive lesions) resulted in categorization of 61 (58%) as thyroid remnant tissue, 16 (26%) with morphologic correlate on CT images and 33 (54%) on MR images; and 29 (27%) with lymph node metastasis, 18 (62%) with morphologic correlate on CT images and 24 (83%) on MR images; and 16 (15%) were categorized as indeterminate. Twenty three lesions were not discernible on CT images but were visible on MR images, 15 of which were smaller than 10 mm, and about two-thirds of which were classified as thyroid remnant tissue. Recalculation of dosimetry based on MR imaging findings for these small lesions would have changed initial therapy in five patients. PET/MR imaging was concluded to be superior to PET/CT for assigning a PET focus to a morphologic correlate, and Iodine 124 PET/MR imaging was found to enhance diagnostic certainty for lesions smaller than 10 mm and to improve pretherapeutic lesion dosimetry in differentiated thyroid carcinomas.

Tatsumi et al (73) retrospectively compared FDG PET/CT with fused PET/MR imaging in 47 patients suspected of having or known to have pancreatic cancer. They reported significantly higher confidence scores of visibility of tumors on T1-weighted MR images compared with those on CT images, and higher (although nonsignificant) diagnostic accuracy of PET/T1-weighted MR imaging (93%) and PET/T2-weighted MR imaging (90.7%) compared with that of PET/CT (88.4%).

Nakajo et al (67) retrospectively compared FDG PET/CT with fused PET/MR imaging in 31 patients with gynecologic tumors. They reported significantly improved detection of uterine and ovarian lesions at T2-weighted MR imaging compared with that at T1-weighted MR imaging and CT and significantly improved FDG localization to lesions with PET/T2-weighted MR imaging compared with PET/T1-weighted MR imaging or PET/CT.

Kim et al (74) retrospectively evaluated the diagnostic performance of FDG PET/CT compared with fused PET/MR imaging for detection of metastatic lymph nodes in 79 patients with stage IB-IVA cervical cancer before surgery. The areas under the receiver operating characteristic curve for PET/CT and PET/MR imaging were 0.690 and 0.735, respectively (P = .045). Overall, fused PET/MR imaging had a higher diagnostic performance than did PET/CT for detection of lymph node metastases in patients with cervical cancer.

For detection and characterization of distant metastases in organs for metastasis staging, PET and MR imaging are complementary to varying degrees, depending on the underlying tumor characteristics such as the degree of metabolism, cell proliferation, and hypoxia present, the size of metastases, and the specific anatomic sites involved. MR imaging generally provides superior performance to that of CT for early detection and characterization of metastases in certain tissues such as the bone marrow (Fig 3), liver (Fig 4), and brain (Fig 5), whereas CT is superior for the evaluation of small lung metastases (75–79).

For example, in a retrospective study of 37 patients with suspected liver metastases by Donati et al (75), the accuracy of lesion detection and diagnostic confidence of FDG PET/CT, gadolinium-ethoxybenzyl-diethylenetriamine pentaacetic acid (Gd-EOB-DTPA)–enhanced MR imaging, and retrospectively fused FDG PET/MR imaging were compared. The detection rate of liver lesions was significantly lower for FDG PET/CT than that for Gd-EOB-DTPA–enhanced MR imaging (64% and 85%, respectively). The sensitivity for detection of liver metastases for FDG PET/CT, Gd-EOB-DTPA–enhanced MR imaging, FDG PET/MR imaging for reader 1, and FDG PET/MR imaging for reader 2, respectively, were 76%, 91%, 93%, and 93%. The specificities for characterization were 90%, 100%, 87%, and 97%. The accuracy percentages were 85%, 94%, 92%, and 96%. The difference in sensitivity between FDG PET/CT and FDG PET/MR imaging was significant, and diagnostic confidence for liver lesions larger than 1 cm was significantly higher for FDG PET/MR imaging than it was for FDG PET/CT, although Gd-EOB-DTPA–enhanced MR imaging and FDG PET/MR imaging did not show significantly different performance for diagnosis.

Similarly, Yong et al (80) retrospectively assessed the sensitivity of CT, MR imaging, FDG PET, fused PET/CT, and fused PET/MR imaging in 24 patients with colorectal cancer that had metastasized to the liver. Lesion-level sensitivities were 64.5%, 80.2%, 54.5%, 84.2%, and 98.3%, respectively. The authors concluded that PET/MR imaging can help detect more metastatic lesions that are smaller than 1 cm than PET/CT($P < .05$) can.

Advanced functional MR imaging techniques such as DW imaging, MR spectroscopy, and perfusion-weighted imaging used with PET can further enhance detection and characterization of malignant lesions for prognosis assessment, biopsy and pretreatment planning, patient selection for certain therapeutic agents, and response prediction and assessment (60,79,81,82).

For example, Laurent et al (83) prospectively compared whole-body MR imaging, including DW imaging, to FDG PET/CT for staging malignant melanoma in 35 patients by using histology, imaging follow-up, or clinical follow-up as reference standards. A total of 120 lesions were detected, 70 of which were malignant. The sensitivity and specificity were 82% and 97% for whole-body MR imaging and 72.8% and 92.7% for FDG PET/

CT, respectively. DW imaging allowed detection of 14 additional malignant lesions (20%) than did standard contrast-enhanced MR imaging, with most lesions involving bone marrow, liver, subcutaneous tissues, and peritoneum.

Kim et al (84) performed a study in 49 patients with non–small cell lung cancer to compare the diagnostic performance of FDG PET/CT with that of FDG PET/CT combined with DW and T2-weighted MR imaging for preoperative detection and characterization of regional lymphadenopathy. They reported a sensitivity, specificity, and accuracy of 46% (18 of 39), 96% (161 of 167), and 87% (179 of 206) for FDG PET/CT alone and 69% (27 of 39), 93% (156 of 167), and 89% (183 of 206) for combined PET/CT and MR imaging. Therefore, the combination of PET/CT and MR imaging significantly improved the detection of nodal metastases, potentially reducing unnecessary open thoracotomies.

Park et al (85) compared DW imaging and FDG PET/CT to predict pathologic complete response in 34 patients with invasive breast cancer who were receiving neoadjuvant chemotherapy. Percentage changes in apparent diffusion coefficient (ADC) and standardized uptake value (SUV) were calculated, and diagnostic performance for predicting pathologic complete response were evaluated by using receiver operating characteristic curve analysis. The areas under the curve for DW imaging, FDG PET/CT, and combined DW imaging and FDG PET/CT were 0.910, 0.873, and 0.944, respectively, and the best cutoffs for differentiating pathologic from nonpathologic complete response were a 54.9% increase in ADC and a 63.9% decrease in SUV. DW imaging showed 100% (7 of 7) sensitivity and 70% (19 of 27) specificity and FDG PET/CT showed 100% (27 of 27) sensitivity and 78% (21 of 27) specificity. DW imaging FDG PET/CT showed a trend toward improved specificity compared with DW imaging alone. The authors concluded that DW imaging and FDG PET/CT show similar diagnostic accuracy for predicting pathologic complete response to neoadjuvant chemotherapy in breast cancer patients, and that DW imaging with FDG PET/CT has the potential to improve specificity in predicting pathologic complete response.

Figure 3

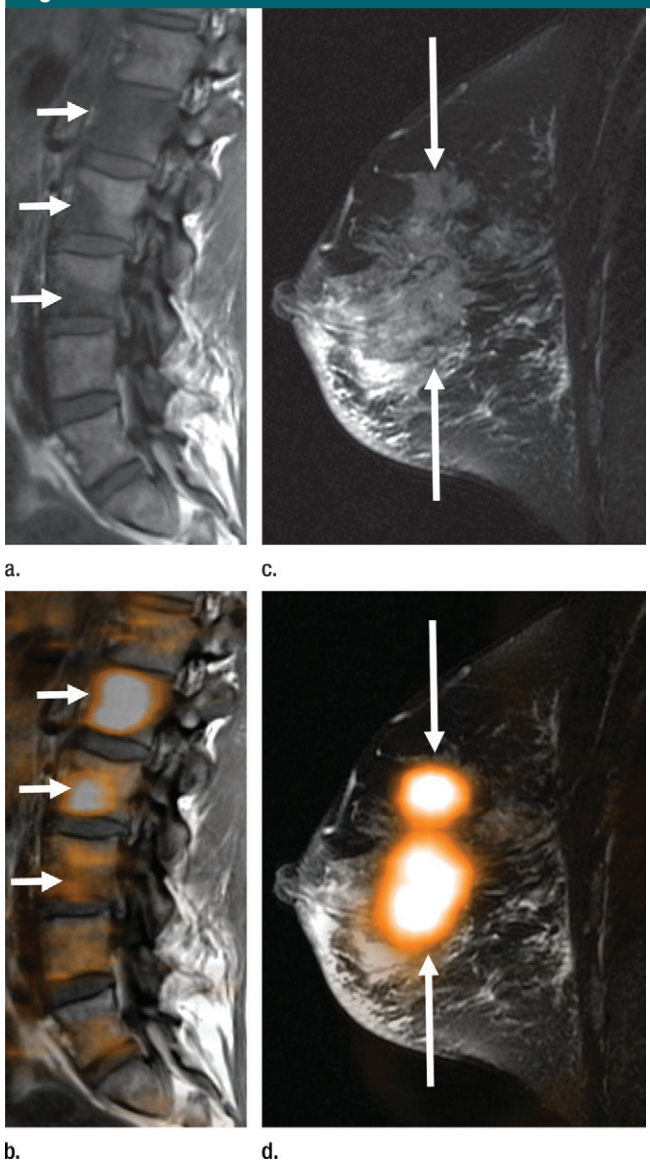

Figure 3: Images in a 40-year-old woman who underwent staging evaluation for invasive ductal breast carcinoma. **(a)** Sagittal 1.5-T fluid-attenuated inversion-recovery T1-weighted fast spin-echo MR image (repetition time msec/echo time msec/inversion time msec, 1800/9.6/860) of lumbar spine shows multiple hypointense foci in vertebral bodies (arrows) due to metastases. **(b)** Software-fused FDG PET/MR image reveals FDG uptake in corresponding lesions (arrows). **(c)** Sagittal 1.5-T fat-suppressed T2-weighted fast spin-echo MR image (3000/90) of breast shows large irregular mass (between arrows). **(d)** Software-fused FDG PET/MR image reveals strong FDG uptake in breast mass (between arrows) consistent with aggressive tumor biology.

Park et al (86) assessed the performance of parametric fusion PET/MR imaging based on carbon 11 (^{11}C)-choline PET/CT and ADC maps derived from DW imaging for identification of primary prostate cancer in 17 patients. Tumor-to-background count density ratios for ^{11}C-choline and ADC, and the quotient of ^{11}C-choline over ADC ($P_{CHOL/ADC}$) were calculated and compared with reference histopathologic results. The tumor-to-background count density ratios for both ^{11}C-choline and $P_{CHOL/ADC}$ were significantly greater in patients with prostate cancer with a Gleason score greater than or equal to 3 + 4 than in those with a Gleason score less than or equal to 3 + 3 and in control subjects, and tumor-to-background count density ratios for ADC were significantly lower in those with a Gleason score greater than or equal to 3 + 4 than in those with a Gleason score less than or equal to 3 + 3. Over-

Figure 4

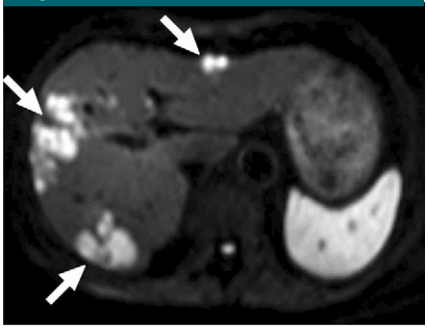

a.

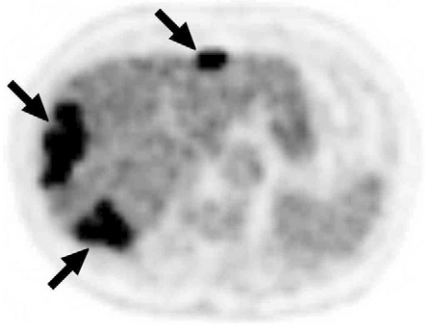

b.

Figure 4: Images in a 61-year-old woman who underwent pretreatment evaluation for colon carcinoma. **(a)** Axial 1.5-T high-*b*-value diffusion-weighted (DW) single-shot spin-echo echoplanar MR image with spectral presaturation with inversion recovery (1522/721/80; *b*= 500 sec/mm^2) in liver shows multiple high–signal-intensity lesions (arrows) due to intralesional restriction of water molecule diffusivity. **(b)** Corresponding FDG-PET image reveals strong FDG uptake in same hepatic lesions (arrows) due to colon cancer metastases.

all, parametric MR imaging by using $P_{CHOL/ADC}$ improved tumor-to-background count density ratios of prostate cancers with Gleason scores greater than or equal to 3 + 4 compared with ^{11}C-choline PET/CT or DW imaging alone, which may improve identification and localization of primary prostate cancers.

PET/MR imaging has the potential to optimize the treatment of patients with various types of cancer before, during, and after therapeutic intervention. Furthermore, PET/MR imaging may be useful for optimizing drug development by noninvasively providing in vivo quantitative data about the pharmacokinetics (absorption, biodistribution, metabolism, and elimination) and pharmacodynamics of novel therapeutic agents of interest (87,88).

Figure 5

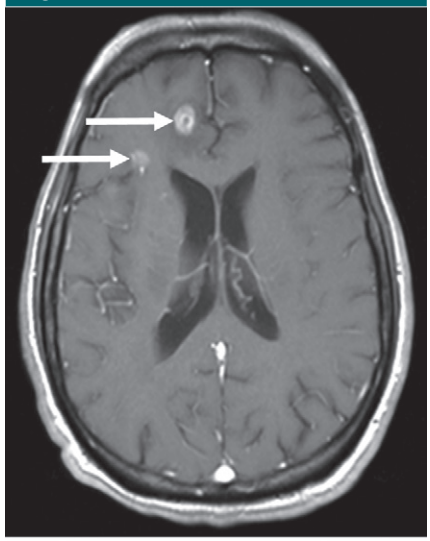

a.

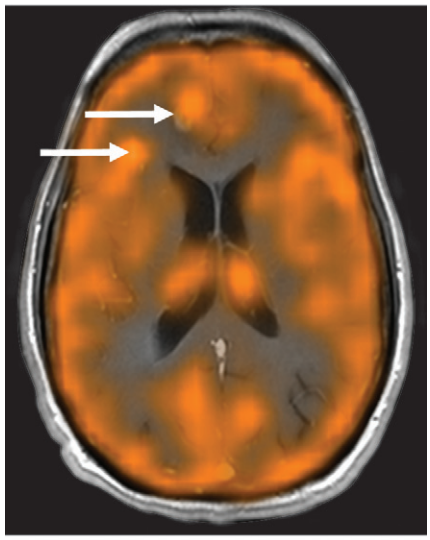

b.

Figure 5: Images in a 59-year-old man who underwent restaging evaluation for melanoma. **(a)** Axial 1.5-T contrast-enhanced T1-weighted fast spin-echo MR image (500/17) in brain demonstrates two enhancing lesions (arrows) at gray-white matter junction in right frontal lobe due to melanoma metastases. **(b)** Software-fused FDG PET/MR image shows FDG uptake in same lesions (arrows), although with suboptimal conspicuity secondary to FDG uptake in subjacent gray matter.

Finally, replacement of PET/CT (total radiation dose of approximately 8–30 mSv depending on CT acquisition parameters, anatomic region of coverage, and radiotracer dose; average dose of approximately 14 mSv after administration of FDG) with PET/MR imaging (average dose of approximately 7–10 mSv after administration of 10–15 mCi [370–555 MBq] of FDG) would reduce radiation exposure, which is highly desirable for all patients, especially for pediatric patients and those who undergo multiple examinations (Fig 6). Simultaneous improvements in PET detector technology and reconstruction techniques may also allow for additional reductions in radiation exposure (89,90).

Neurologic Disease

PET/MR imaging has the potential to provide integrated multidimensional and multiparametric structural and functional assessment of the central nervous system in patients with neurodegenerative, ischemic, vascular, neurologic-oncologic, traumatic, psychiatric, behavioral, seizure-related, and age-related conditions and may be useful for assessment of treatments including cellular and gene therapies (65,91,92). This is, in part, related to the wide variety of available PET radiotracers that can be used to probe biologic properties of brain tissue and complementary functional MR imaging techniques (42,60,93). High degrees of spatial and temporal coregistration of PET and MR imaging datasets are feasible, allowing for evaluation of biologic processes such as metabolism, perfusion, oxygen consumption, receptor expression, and function in even the smallest neurologic-anatomic structures (94,95). This is particularly relevant in neurologic oncology, in which accurate alignment of structural and functional information is essential for biopsy and treatment planning. MR imaging can also allow for partial volume correction of PET emission data to provide the most accurate PET quantification of disease (96,97). Some examples of the potential clinical uses of PET/MR imaging for neurologic disease assessment are as follows.

In a study by Boss et al (94) with 10 patients with intracranial masses, simultaneous PET/MR imaging was performed after PET/CT with either ^{11}C-methionine (glial tumors) or gallium 68 (^{68}Ga)-D-phenylalanine(1)-tyrosine(3)-octreotide (meningiomas). Ratios of tumor to gray matter and tumor to white matter were calculated for gliomas, and radiotracer uptake of meningiomas was referenced to that of nasal mucosa. In all patients, PET datasets showed similar diagnostic image quality from PET/MR and PET/CT studies, although slight streak artifacts were visible on coronal and sagittal images when the PET/MR imaging insert was used. However, image prefiltering with a 4-mm Gaussian filter at a resolution comparable to that of PET/CT virtually eliminated these artifacts. Tumor-to-reference count density tissue ratios exhibited excellent concordance between PET/MR imaging and PET/CT (R = 0.98; mean paired relative error, 7.9% ± 12.2%). No major artifacts or distortions were detected in MR images from PET/MR imaging. The authors concluded that structural, functional, and molecular imaging of patients with brain tumors is feasible with diagnostic image quality by using simultaneous PET/MR imaging.

Similarly, Schwenzer et al (98) studied 50 patients with intracranial masses, head and upper neck tumors, or neurodegenerative diseases by using simultaneous PET/MR imaging at 3 T after FDG PET/CT, ^{11}C-methionine, or ^{68}Ga-D-phenylalanine(1)-tyrosine(3)-octreotide. PET/MR imaging was successful in 45 of 50 patients, and demonstrated high concordance with PET/CT results for image quality, tumor delineation, frontal and parietal-occipital ratios, and left-right asymmetry index, although SUVs were not compared. Two of five studies were unsuccessful due to patient-related factors, whereas three of five studies were unsuccessful due to technical problems (unstable PET detector temperature or problems with the PET insert mounting device). Arterial spin labeling and hydrogen 1 MR spectroscopy were feasible in all patients who underwent these techniques, and dental artifacts led to one nondiagnostic diffusion-tensor imaging dataset.

Figure 6

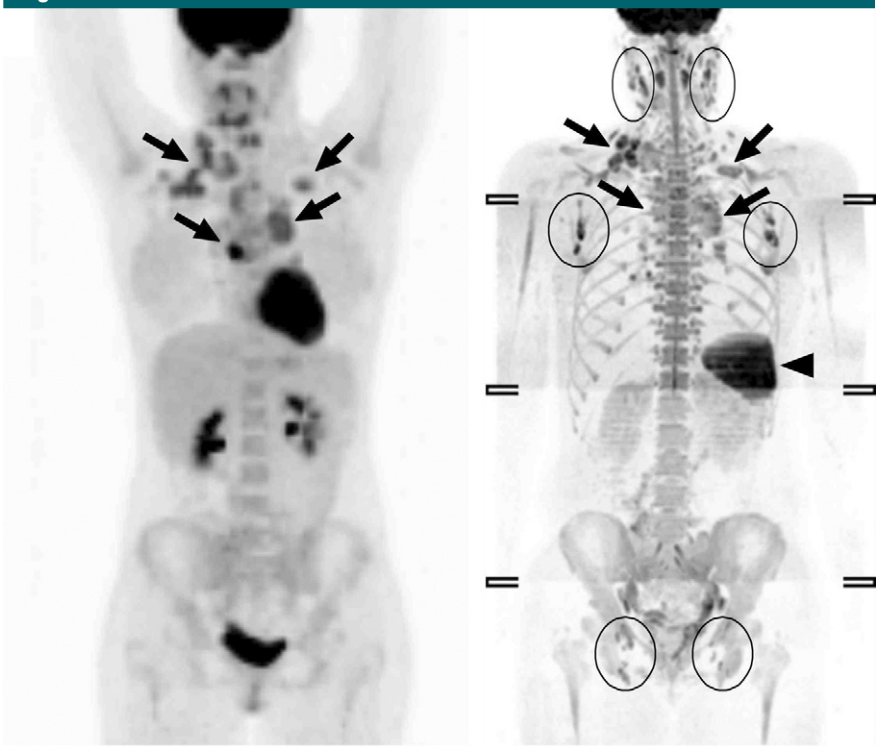

a. b.

Figure 6: Images in a 16-year-old girl who underwent staging evaluation for Hodgkin lymphoma. **(a)** Coronal maximum intensity projection FDG PET image shows FDG uptake in right cervical, right supraclavicular, bilateral infraclavicular, left hilar, and mediastinal lymph nodes (arrows), indicating Ann Arbor stage II disease. **(b)** Coronal 1.5-T maximum intensity projection grayscale inverted high-*b*-value DW single-shot spin-echo echoplanar MR image with spectral presaturation with inversion recovery (8612/78/180; b = 1000 sec/mm^2) reveals involvement of same nodal sites (arrows). Note normal high signal intensity of spleen (arrowhead) and normal nonlymphomatous lymph nodes in neck, axillary regions, and inguinal regions (circled).

A study by Cho et al (95) of five healthy volunteers showed that sequential FDG-PET and 7.0-T MR imaging allowed for measurement of glucose metabolism in hippocampal substructures, with the dentate gyrus and cornu ammonis showing the highest glucose uptake. This approach may provide a new tool for future investigation of related brain diseases (Fig 7a, 7b). In another study by Cho et al (99) of five volunteers, sequential PET/MR imaging clearly demonstrated the fine anatomic structure of the thalamus and allowed for measurement of glucose metabolism in individual thalamic nuclei, with the medial dorsal thalamic nucleus consistently showing the highest glucose uptake among thalamic nuclei (Fig 7c, 7d). More recently, Cho et al (100) have also shown that FDG PET/MR imaging can be used to visualize the individual raphe nucleus groups (B1-B5) in the brainstem, which in the past were only visible with in vitro histologic studies, and to quantify their glucose metabolism (Fig 7e, 7f), (101).

PET/MR imaging can be useful for the detection of seizure foci before surgery, and for measurement of metabolic activity, neurotransmitter concentration, and enzyme expression in small structures of the brain (102,103). For example, Salamon et al (104) reported that multimodality presurgical evaluation including FDG PET/MR imaging

Figure 7

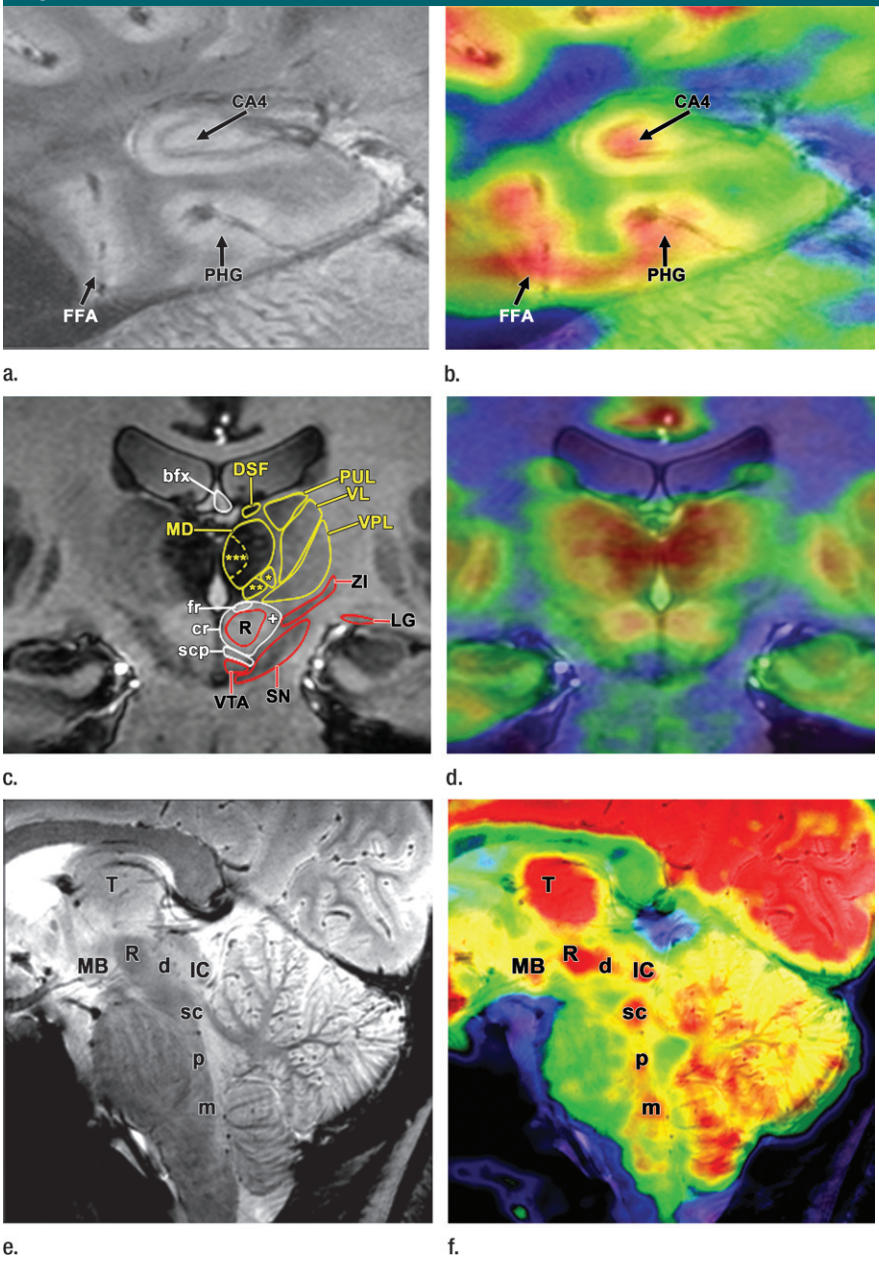

Figure 7: MR and fused PET/MR high-spatial-resolution images of three 23-year-old volunteers, two men and one woman, acquired with the same PET imager (Siemens Healthcare). **(a)** In first male volunteer, coronal 7-T T2*-weighted gradient-echo MR image (750/21; flip angle, 30°) and **(b)** fused PET/MR image of hippocampal region show subhippocampal resolution separating metabolic function of region cornu ammonis 4 *(CA4)* from surrounding structures including parahippocampal gyrus *(PHG)* and fusiform face area *(FFA)*. **(c)** In second male volunteer, coronal 7-T T1-weighted three-dimensional magnetization-prepared rapid-acquisition gradient-echo MR image (4000/5.3/1000; flip angle 10°) and **(d)** fused PET/MR image of thalamic region show subthalamic resolution, allowing for structural and anatomic quantification of individual nuclei. Thalamic nuclei (yellow): centromedian thalamic nucleus (*), parafascicular thalamic nucleus (**), magnocellular part of medial dorsal thalamic nucleus (***), medial dorsal thalamic nucleus *(MD)*, dorsal superficial nucleus *(DSF)*, pulvinar *(PUL)*, ventral lateral thalamic nucleus *(VL)*, ventral posterior lateral thalamic nucleus *(VPL)*. Fiber tracts (white): superior cerebellar peduncle *(scp)*, capsule of red nucleus *(cr)*, fasciculus retroflexus *(fr)*, body of fornix *(bfx)*, cerebellorubrothalamic fibers (+). Other structures (red): lateral geniculate nucleus *(LG)*, zona incerta *(ZI)*, substantia nigra *(SN)*, ventral tegmental area *(VTA)*, red nucleus *(R)*. **(e)** In female volunteer, midline sagittal 7-T T2*-weighted gradient-echo MR image (750/16.8; flip angle, 30°) and **(f)** fused PET/MR image through brainstem show detailed anatomy and metabolic function of raphe nuclei. Raphe nuclei: dorsal *(d)*, superior central *(sc)*, pontine *(p)*, medullary (including magnus, obscurus, and pallidus) *(m)*. mamillary body *(MB)*, thalamus *(T)*, red nucleus *(R)*, inferior colliculus *(IC)*.

enhances noninvasive identification and successful surgical treatment of patients with cortical dysplasia, especially for patients with nonconcordant findings and those with normal MR imaging examinations with mild type I cortical dysplasia.

DW imaging with PET measurements of oxygen consumption and perfusion can be useful for differentiation of intravascular perfusion, tissue blood flow, penumbra, and irreversible tissue damage in ischemic and vascular disease (93). DW imaging can also be applied with PET to detect, characterize, and monitor changes in brain tumors after therapeutic intervention (64). Diffusion-tensor imaging, which provides exquisite detail of the white matter bundles, can be particularly useful for pretreatment planning of brain tumors because it allows separation of peritumoral edema from the infiltrative tumor, pretreatment assessment of white matter tract involvement by tumor, and intraoperative visualization and localization of major white matter tracts to decrease the chance of injury to normal tissues (105,106). For example, Boss et al (106) investigated the possibility of diffusion-tensor imaging with a simultaneous PET/MR imaging system in seven healthy volunteers and four patients with brain tumors. Although stronger rim artifacts were found on fractional anisotropic images computed from dif-

fusion-tensor imaging during simultaneous PET acquisition, no notable differences were found in computation of the direction of the principal eigenvector and fractional anisotropic values at region of interest analysis. In the four patients, diffusion-tensor imaging provided information on displacement and integrity of peritumoral fiber tracts. Therefore, diffusion-tensor imaging may be combined with simultaneous PET data acquisition, offering additional important morphologic and functional information for treatment planning in patients with brain tumors (106).

Perfusion-weighted imaging with PET also may be useful to assess ischemic or vascular, neurodegenerative, and neoplastic brain disorders (Fig 8). Functional MR imaging can be used to preoperatively map the functional cerebral cortex and to identify areas of the cerebral cortex in relation to brain neoplasms, potentially reducing the time of surgery and minimizing intraoperative cortical stimulation methods used during surgical resection (107,108). It can also be used with PET for comparative activation studies, for assessment of activation effects on transmitter release or receptor binding, and for studying the effects of drug usage and withdrawal (94).

Finally, PET/MR imaging may be useful for evaluation of abnormalities of the spinal cord and peripheral nerve disease. For example, Behera et al (109) reported that rats with neuropathic pain showed increased FDG uptake in the affected nerve, and that PET/MR imaging (small animal) can be used effectively to localize FDG uptake in peripheral nerves.

Cardiovascular Disease

PET/MR imaging has potential for clinical assessment of myocardial viability and infarction, ventricular function, cardiomyopathy, myocarditis, pericarditis, atherosclerosis, vasculitis, and other cardiovascular pathologies. This is, in part, due to the wide array of available MR imaging pulse sequences for imaging of cardiovascular structure and function, along with multiple available PET radiotracers to probe molecular processes of interest. Furthermore, MR imaging allows accurate measurement of cardiac chambers, wall thickness, wall motion, and vessel diameters; provides quantitative measures of flow; is useful to assess myocardial perfusion with pharmacological stress testing; and can allow detection and quantification of myocardial fibrosis (Fig 9). Respiratory-gated and electrocardiogram-gated MR imaging may further improve cardiac PET quantification by correcting for misregistration, partial volume effect, and bulk motion (110). As an example of PET/MR imaging application for cardiac assessment, Bengel et al (111) reported that ^{11}C-hydroxyephedrine PET with high spatial resolution MR imaging of structural and wall motion can be useful for delineation of cardiac regional innervation and control mechanisms in patients with dilated cardiomyopathy or after cardiac transplantation.

MR imaging is also useful to show the precise anatomic extent and loca-

Figure 8

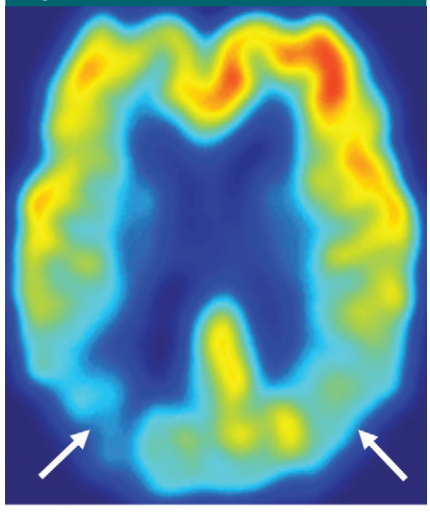

a.

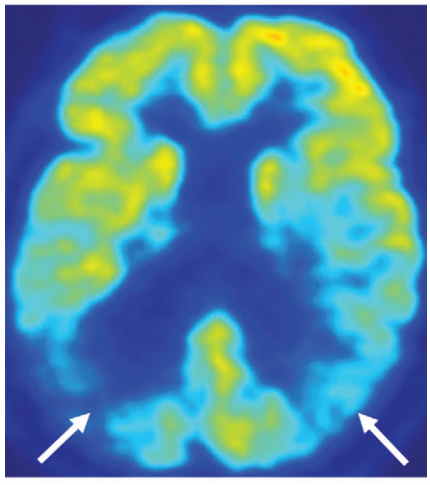

b.

Figure 8: Images in a 67-year-old man with Alzheimer disease. **(a)** Axial 3-T arterial spin-labeling magnetization-prepared rapid acquisition gradient-echo echo-planar MR image (4000/17) and **(b)** corresponding FDG PET image of brain show regions of decreased signal intensity in bilateral parietal gray matter (arrows), with right side greater than left, in keeping with decreased hypoperfusion and hypometabolism, respectively.

Figure 9

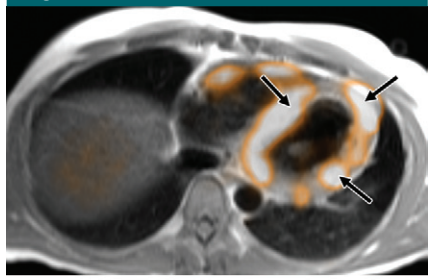

a.

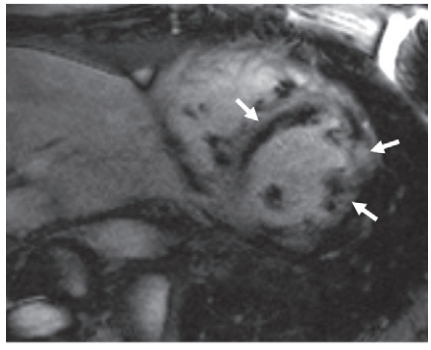

b.

Figure 9: Images in a 51-year-old man with history of cardiac dysrhythmias and sarcoidosis who underwent evaluation for cardiac involvement. **(a)** Axial software-fused FDG PET/MR image of heart demonstrates heterogeneously increased FDG uptake (arrows) in left ventricular myocardium. **(b)** Short-axis 1.5-T delayed-phase postcontrast phase-sensitive inversion-recovery gradient-echo MR image (1077/3.2/250; flip angle, 25°) of heart reveals heterogeneous regions of delayed enhancement (arrows) in mid- and subepicardial portions of left ventricular myocardium, in keeping with granulomatous and/or fibrotic tissue.

Figure 10

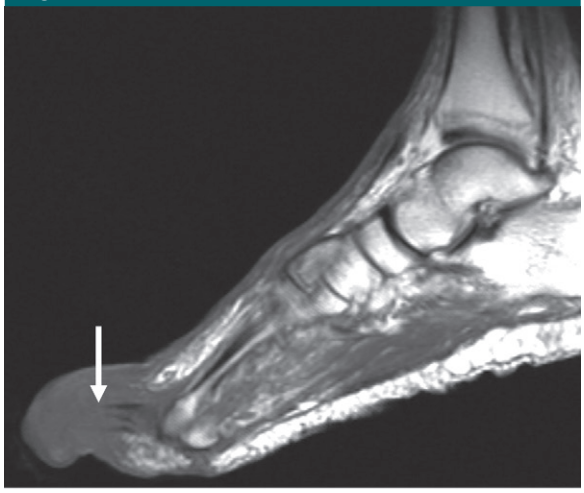

a.

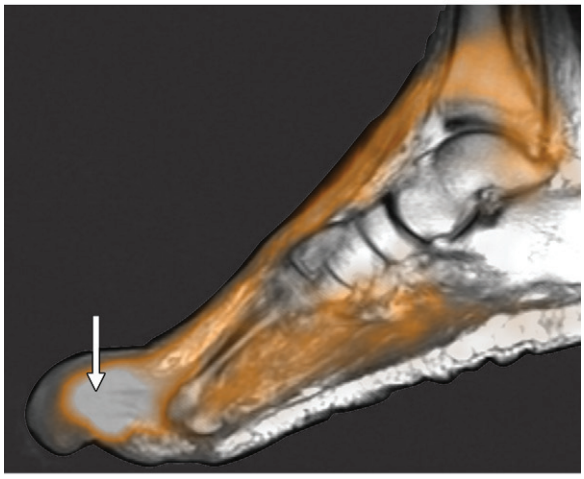

b.

Figure 10: Images in a 58-year-old man with history of diabetes mellitus and toe ulcer who underwent evaluation for osteomyelitis. **(a)** Sagittal 1.5-T T1-weighted fast spin-echo MR image (400/12) of foot shows cortical destruction of second distal phalanx (arrow) with associated decreased bone marrow and soft-tissue signal intensity due to acute osteomyelitis and cellulitis, respectively. **(b)** Software-fused FDG PET/MR image shows corresponding strong FDG uptake (arrow) due to active infection and inflammation.

Table 1

Clinical Applications of PET/MR Imaging

Category	Potential Clinical Applications
Oncologic	Tumor detection, local-regional assessment (tumor and node staging), assessment for distant metastases (metastasis staging), and volume delineation of tumors in areas where tissue contrast with CT is suboptimal (eg, brain, head and neck, spinal cord, peripheral nerves, liver, pelvic organs, breasts, and musculoskeletal system)
	Combination of advanced functional MR imaging techniques with PET for improved detection and characterization of tumors for prognosis assessment, biopsy and pretreatment planning, patient selection for certain therapeutic agents, response prediction and assessment, and optimization of drug development
	Possible first-line imaging modality for evaluation of certain cancers in patients in whom radiation exposure is an issue (eg, children, pregnant patients, patients undergoing multiple repeated examinations)
Neurologic	Multiparametric structural and functional quantitative assessment of the normal central and peripheral nervous system and of various neurodegenerative, ischemic/vascular, neurologic-oncologic, traumatic, psychiatric, behavioral, seizure-related, congenital, and age-related conditions
	Assessment of novel treatments including cellular and gene therapies
Cardiovascular	Multiparametric structural and functional quantitative assessment of myocardial viability and infarction, ventricular function, cardiomyopathy, myocarditis, atherosclerotic disease (regionally and globally), vasculitis, and other cardiovascular pathologies
	Detection, localization, delineation, characterization, and response assessment of cardiac and pericardiac tumors
Musculoskeletal	Complementary roles of PET and MR imaging for optimized diagnosis and response assessment in a wide variety of musculoskeletal disorders (eg, Charcot neuroarthropathy, osteomyelitis, and soft-tissue infection in the diabetic foot, spinal disorders, arthritides)

tion of cardiac and pericardiac tumors, and to characterize their gross composition, which is complementary with FDG PET for response assessment purposes (110,112,113). PET/MR imaging may be important in assessment of cellular and gene therapies, such as in cardiac stem cell transplantation (114). Finally, PET/MR imaging of the vascular system may be useful for regional and global detection, characterization, and quantification of atherosclerotic disease for purposes of risk assessment and drug response assessment, because it can simultaneously provide information about vascular wall thickness, wall inflammation, plaque vulnerability, and degree of luminal narrowing (110,115–117). For example, Fayad et al (117) reported the results of a randomized clinical trial to study the safety and efficacy of dalcetrapib on atherosclerotic disease based on a combination of MR imaging–derived change in total vessel area and FDG PET/CT-derived change in vessel target-to-background ratio.

Musculoskeletal Disease

PET/MR imaging may be important in the assessment of patients with a wide array of musculoskeletal disorders, because MR imaging provides excellent soft-tissue contrast for structural assessment of bone marrow, muscles, tendons, ligaments, cartilaginous structures, and fat (64). For example, FDG PET and MR imaging are synergistic for

Table 2

PET Radiotracers for Evaluation of Biologic Processes or Molecular Targets of Interest

PET Radiotracer	Biologic Process/Molecular Target of Interest
FDG*	Glucose metabolism
Carbon 11 (^{11}C)-thymidine	Cell proliferation
3′-Deoxy-3′-^{18}F-fluorothymidine	Cell proliferation
^{11}C-choline*	Choline kinase activity/synthesis of membrane phospholipids
^{18}F-fluorocholine	Choline kinase activity/synthesis of membrane phospholipids
L-[methyl-^{11}C]methionine	Amino acid metabolism
O-(2-^{18}F-fluoroethyl)-L-tyrosine	Amino acid metabolism
^{18}F-6-fluorodihydroxyphenylalanine	Amino acid metabolism
^{18}F-fluoromisonidazole	Hypoxia
Copper 64 (II)-diacetyl-bis (N4-methylthiosemicarbazone)	Hypoxia
^{18}F-2-(2-nitro-hydrogen 1-imidazol-1-yl)-*N*-(2,2,3,3,3-pentafluoropropyl)-acetamide	Hypoxia
^{18}F-galacto-arginine-glycine-aspartate	Angiogenesis
4-^{18}F-fluorobenzoyl-annexin V	Apoptosis
^{11}C-acetate	Myocardial oxidative metabolism
^{11}C-palmitate	Myocardial fatty acid metabolism
Nitrogen 13-ammonia*	Blood flow
Oxygen 15-water	Blood flow
Rubidium 82-chloride*	Blood flow
^{18}F-sodium fluoride (^{18}F-NaF)*	Bone metabolism/calcification
Gallium 68 (^{68}Ga)-DOTA-Phe^{1}-Tyr^{3}-octreotide	Somatostatin receptors
Gluc-Lys (^{18}F-fluoropropionyl-TOCA)	Somatostatin receptors
^{68}Ga-DOTA-Tyr^{3}-Thr^{8}-octreotide	Somatostatin receptors
^{68}Ga-DOTA-1-NaI$_3$-octreotide	Somatostatin receptors
16α-^{18}F-fluoroestradiol-17β	Estrogen receptors

Note.—Radiotracers listed are a small selection of the many available.

*US Food and Drug Administration-approved radiotracers

detection and characterization of complications of the foot in patients with diabetes, such as Charcot neuroarthropathy, osteomyelitis, and soft-tissue infection. In particular, Basu et al (118) showed in a series of 63 patients that there was a significant difference between the degree of FDG uptake in an uncomplicated diabetic foot, a foot with Charcot neuroarthropathy, and a foot with osteomyelitis, and that the sensitivity and accuracy for diagnosis of Charcot neuroarthropathy were 100% and 94% for FDG PET and 77% and 75% for MR imaging, respectively. Furthermore, Nawaz et al (119) reported that, in a series of 110 patients with a complicated diabetic foot, FDG PET had a sensitivity, specificity, and accuracy of 81%, 93%, and 90%, for the diagnosis of osteomyelitis, and 91%, 78%, and 81% for MR imaging, respectively, demonstrating that FDG PET and MR imaging provide complementary information for these conditions (Fig 10). In addition, PET and MR imaging are complementary for the evaluation of various arthritides and for treatment monitoring, may be useful to depict meniscal tears with associated synovitis, and can provide for accurate quantitative assessment of the bone marrow in normal and abnormal states (64,120–123).

See Table 1 for a summary of the potential clinical applications of PET/MR imaging according to different categories. Also see Table 2 for a sampling of different PET radiotracers available for evaluation of different biologic processes or molecular targets of interest, and Table 3 for a listing of available functional MR imaging methods with potential applications.

PET/MR Image Segmentation and Global Disease Assessment

In the context of quantitative PET/MR imaging, (semi)automated image segmentation may be useful for many clinical applications such as estimation of normal and abnormal tissue volumes, extraction of other clinically relevant parameters of interest, and partial volume correction of PET measures of radiotracer uptake in tissues of interest because it is generally associated with improved accuracy, precision, and efficiency related to manual segmentation (77,96). Global disease assessment through combined molecular and volumetric measurements of all disease sites also will be important in the quantification of disease for pretreatment planning, prognosis, and prediction and assessment of treatment response (77). Reports of the clinical use of image segmentation and global disease assessment with PET and MR imaging are highlighted as follows.

Alavi et al (97) calculated the total brain metabolism as the product of brain volume (obtained by means of computer-assisted segmentation of cerebrospinal fluid and brain at MR imaging [124]) and partial volume-corrected average brain metabolic rate (based on FDG PET and MR imaging–based tissue segmentation for partial volume correction) in 20 patients with Alzheimer disease and 17 age-matched control subjects. They showed that partial volume-corrected metabolic rates per unit of weight of brain were not significantly different between these two cohorts, but that total brain metabolism was significantly lower in patients with Alzheimer disease and could be useful as a sensitive correlate for cognitive dysfunction. Bural et al (125) reported that hepatic metabolic volumetric product (calculated as the product of FDG-PET based hepatic SUV and MR imaging–based hepatic volume) and SUV were significantly greater in patients with diffuse hepatic steatosis compared with those in control patients, which is con-

Table 3

Functional MR Imaging Methods, Characteristics, and Applications

MR Imaging Method	Characteristics	Potential Applications
Diffusion-tensor imaging	Measurement of directionality of water diffusion fractional anisotropy; ranging from 0 (isotropic) to 1 (maximally anisotropic)	Assessment of white matter tracts, peripheral nerves and skeletal muscles
DW imaging	Measurement of diffusivity of water molecules	Detection of acute ischemia; tumor detection, characterization, localization, staging, response prediction, and treatment monitoring; detection and characterization of inflammatory conditions (eg, inflammatory bowel disease)
Functional MR imaging	Demonstration of blood oxygenation changes with blood oxygenation level–dependent contrast or perfusion changes with arterial spin labeling contrast	Characterization of functional anatomy in the brain (eg, for neurosurgical treatment planning)
MR elastography	Quantitative assessment of the shear modulus (or stiffness) of tissues	Assessment of hepatic fibrosis, tumors of the breast (eg, potentially complementary to detection with contrast-enhanced MR imaging), and of other organs (eg, bone, brain, cartilage, globe, heart, heel fat pads, kidney, lungs, pancreas, prostate, skeletal muscle, spinal cord, spleen)
MR spectroscopy	Detection of various molecules present at concentrations in millimoles per liter.	Tumor detection, localization, characterization, grading, and response assessment
Perfusion-weighted imaging	Assessment of perfusion values (eg, relative blood flow, relative blood volume, mean transit time, microvessel permeability [K^{trans}]) with dynamic contrast-enhanced T1-weighted or T2*-weighted methods or with arterial spin labeling (which takes advantage of arterial water as a freely diffusible tracer)	Diagnosis, prognosis, and response assessment of cerebrovascular disease; tumor detection, localization, characterization, grading, staging, response prediction, and treatment monitoring (including antiangiogenic therapies)
Very short echo time imaging	Imaging of tissues with very short T2*	Evaluation of short T2* tissues such as lung parenchyma, tendons, ligaments, periosteum, and cortical bone; and evaluation of conditions that increase the concentration of short T2 components such as fibrosis, iron deposition, some stages of hemorrhage, and various deposition diseases (eg, amyloidosis)

Note.—Methods listed are a representative subst of those available.

sistent with the presence of active hepatic inflammation. Basu et al (126) reported the feasibility of MR imaging–based bone marrow segmentation by using available software techniques for quantitative calculation of pure red marrow metabolism at FDG PET, which may be clinically useful for evaluation of benign and malignant bone marrow disorders. Nawaz et al (127) studied 27 patients with diabetes who underwent lower-extremity FDG PET and MR imaging. The popliteal artery–to-background ratio (measured at FDG PET) and whole-foot metabolic volumetric product (calculated as the product of PET-based foot SUV and MR imaging–based foot volume measurements) were then assessed in all subjects. Popliteal artery–to-background ratio and whole-foot metabolic volumetric product were shown to be significantly correlated (r = 0.73), indicating that as popliteal arterial atherosclerosis increases, foot metabolism also increases, presumably because of increased glycolysis related to chronic ischemia.

Challenges Relevant to PET/MR Imaging

Despite the many promising aspects of PET/MR imaging, challenges beyond those of a technical nature remain and must be addressed before routine clinical implementation (128,129). Comparative effectiveness research is required to justify the need for concurrent PET/MR imaging relative to software-based PET/MR imaging fusion, PET/CT, or MR imaging alone because these three are already adequate in many clinical scenarios and are less expensive and logistically and operationally less complex. Cost-effectiveness comparisons between concurrent and sequential PET/MR imaging are also needed (57,58). More biologic studies to investigate the safety of PET radiotracers with MR imaging should also be conducted, because results of a few studies have shown that

static and low-frequency magnetic fields may enhance the genotoxic potential of ionizing radiation (129–134). In addition, although higher field strength (ie, 7.0 T) PET/MR imaging is feasible to improve delineation of fine anatomic structure and to improve functional MR imaging capabilities, further research on potential adverse effects and cost effectiveness will be required (36,58,135,136). Studies to assess the benefits of radiation dose reduction with PET/MR imaging relative to PET/CT are also warranted. Standardized appropriateness criteria, image acquisition parameters, and radiotracer and contrast material–injection protocols for PET/MR imaging must be established and disseminated for optimized evaluation of specific patient populations, disease conditions, and body parts of interest, and new procedural, safety, and quality-control guidelines for clinical use of PET/MR imaging will also be needed. Furthermore, requisite qualifications for interpreting physicians, residents in training, technologists, and medical physicists must be defined by groups such as the Society of Nuclear Medicine and the American College of Radiology, among others. Finally, new Medicare reimbursement guidelines for PET/MR imaging must be established before clinical implementation.

Summary

PET/MR imaging offers the potential for a powerful "one-stop shop" combination of structural, functional, and molecular imaging technology that may be superior to that of PET/CT, PET alone, or MR imaging alone for certain clinical applications. Future research to evaluate the most appropriate clinical applications of PET/MR imaging on the basis of diagnostic performance, technical feasibility, practicality, and cost in relation to existing diagnostic techniques will therefore be required before routine clinical PET/MR imaging can become a reality.

Disclosures of Conflicts of Interest: D.A.T. No potential conflicts of interest to disclose. **H.Z.** No potential conflicts of interest to disclose. **T.C.K.** No potential conflicts of interest to disclose. **B.S.** No potential conflicts of interest to disclose. **J.K.U.** No potential conflicts of interest to disclose. **Z.H.C.** Financial activities related to the present article: Institution received a grant from the Neuroscience Research Institute, Gachon University. Financial activities not related to the present article: none to disclose. Other relationships: none to disclose. **A.A.** No potential conflicts of interest to disclose.

References

1. Zaidi H, Mawlawi O, Orton CG. Point/counterpoint. Simultaneous PET/MR will replace PET/CT as the molecular multimodality imaging platform of choice. Med Phys 2007;34(5):1525–1528.
2. Zaidi H, Montandon ML, Alavi A. The clinical role of fusion imaging using PET, CT, and MR imaging. Magn Reson Imaging Clin N Am 2010;18(1):133–149.
3. Pietrzyk U. Does PET/CT render software fusion obsolete? Nuklearmedizin 2005; 44(Suppl 1):S13–S17.
4. Weigert M, Pietrzyk U, Müller S, Palm C, Beyer T. Whole-body PET/CT imaging: combining software- and hardware-based co-registration. Z Med Phys 2008;18(1):59–66.
5. Nehmeh SA, Erdi YE. Respiratory motion in positron emission tomography/computed tomography: a review. Semin Nucl Med 2008;38(3):167–176.
6. Slomka PJ, Baum RP. Multimodality image registration with software: state-of-the-art. Eur J Nucl Med Mol Imaging 2009; 36(Suppl 1):S44–S55.
7. Klein S, Staring M, Murphy K, Viergever MA, Pluim JPW. elastix: a toolbox for intensity-based medical image registration. IEEE Trans Med Imaging 2010;29(1):196–205.
8. Hill DL, Batchelor PG, Holden M, Hawkes DJ. Medical image registration. Phys Med Biol 2001;46(3):R1–R45.
9. Maes F, Vandermeulen D, Suetens P. Medical image registration using mutual information. Proc IEEE 2003;91(10):1699–1722.
10. Hutton BF, Braun M. Software for image registration: algorithms, accuracy, efficacy. Semin Nucl Med 2003;33(3):180–192.
11. Hill A, Cootes TF, Taylor CJ, Lindley K. Medical image interpretation: a generic approach using deformable templates. Med Inform (Lond) 1994;19(1):47–59.
12. Maes F, Collignon A, Vandermeulen D, Marchal G, Suetens P. Multimodality image registration by maximization of mutual information. IEEE Trans Med Imaging 1997; 16(2):187–198.
13. Lau YH, Braun M, Hutton BF. Non-rigid image registration using a median-filtered coarse-to-fine displacement field and a symmetric correlation ratio. Phys Med Biol 2001;46(4):1297–1319.
14. Juweid ME, Stroobants S, Hoekstra OS, et al. Use of positron emission tomography for response assessment of lymphoma: consensus of the Imaging Subcommittee of International Harmonization Project in Lymphoma. J Clin Oncol 2007;25(5):571–578.
15. Weber WA. Assessing tumor response to therapy. J Nucl Med 2009;50(Suppl 1): 1S–10S.
16. De Moor K, Nuyts J, Plessers L, Stroobants S, Maes F, Dupont P. Non-rigid registration with position dependent rigidity for whole body PET follow-up studies. Proc IEEE Nuclear Science Symposium and Medical Imaging Conference 2006; 3502–3506.
17. Zaidi H, Ojha N, Morich M, et al. Design and performance evaluation of a whole-body Ingenuity TF PET-MRI system. Phys Med Biol 2011;56(10):3091–3106.
18. Veit-Haibach P, Kuhn FP, Wiesinger F, Delso G, von Schulthess G. PET-MR imaging using a tri-modality PET/CT-MR system with a dedicated shuttle in clinical routine. MAGMA 2012 Oct 9. [Epub ahead of print].
19. Cho ZH, Son YD, Kim HK, et al. A fusion PET-MRI system with a high-resolution research tomograph-PET and ultra-high field 7.0 T-MRI for the molecular-genetic imaging of the brain. Proteomics 2008;8(6): 1302–1323.
20. Zaidi H, Del Guerra A. An outlook on future design of hybrid PET/MRI systems. Med Phys 2011;38(10):5667–5689.
21. Klose U. In vivo proton spectroscopy in presence of eddy currents. Magn Reson Med 1990;14(1):26–30.
22. Camacho CR, Plewes DB, Henkelman RM. Nonsusceptibility artifacts due to metallic objects in MR imaging. J Magn Reson Imaging 1995;5(1):75–88.
23. Delso G, Fürst S, Jakoby B, et al. Performance measurements of the Siemens mMR integrated whole-body PET/MR scanner. J Nucl Med 2011;52(12):1914–1922.
24. Christensen NL, Hammer BE, Heil BG, Fetterly K. Positron emission tomography within a magnetic field using photomultiplier tubes and lightguides. Phys Med Biol 1995;40(4):691–697.
25. Catana C, Wu Y, Judenhofer MS, Qi J, Pichler BJ, Cherry SR. Simultaneous acquisition of multislice PET and MR images: initial results with a MR-compatible PET scanner. J Nucl Med 2006;47(12):1968–1976.
26. Lucas AJ, Hawkes RC, Ansorge RE, et al. Development of a combined microPET-MR system. Technol Cancer Res Treat 2006; 5(4):337–341.

27. Kim JS, Lee JS, Im KC, et al. Performance measurement of the microPET focus 120 scanner. J Nucl Med 2007;48(9):1527–1535.

28. Shao Y, Cherry SR, Farahani K, et al. Simultaneous PET and MR imaging. Phys Med Biol 1997;42(10):1965–1970.

29. Pichler B, Lorenz E, Mirzoyan R, Pimpl W, Roder F, Schwaiger M. Performance tests of a LSO-APD PET module in a 9.4 Tesla magnet. IEEE Nuclear Science Symposium and Medical Imaging Conference Record 1997; 1237–1239.

30. Marsden PK, Strul D, Keevil SF, Williams SC, Cash D. Simultaneous PET and NMR. Br J Radiol 2002;75(Spec No):S53–S59.

31. Cherry SR. Multimodality in vivo imaging systems: twice the power or double the trouble? Annu Rev Biomed Eng 2006;8:35–62.

32. Cherry SR, Louie AY, Jacobs RE. The Integration of Positron Emission Tomography with Magnetic Resonance Imaging. Proc IEEE 2008;96(3):416–438.

33. Pichler BJ, Judenhofer MS, Catana C, et al. Performance test of an LSO-APD detector in a 7-T MRI scanner for simultaneous PET/MRI. J Nucl Med 2006;47(4):639–647.

34. Schlyer D, Vaska P, Tomasi D, et al. A simultaneous PET/MRI scanner based on the RatCAP in small animals. IEEE Nucl Sci Symp Conf Rec 2007; 3256–3259.

35. Woody C, Schlyer D, Vaska P, et al. Preliminary studies of a simultaneous PET/MRI scanner based on the RatCAP small animal tomograph. Nucl Instr Meth A. 2007;571(1-2):102–105.

36. Judenhofer MS, Catana C, Swann BK, et al. PET/MR images acquired with a compact MR-compatible PET detector in a 7-T magnet. Radiology 2007;244(3):807–814.

37. Judenhofer MS, Wehrl HF, Newport DF, et al. Simultaneous PET-MRI: a new approach for functional and morphological imaging. Nat Med 2008;14(4):459–465.

38. Ravindranath B, Junnarkar SS, Purschke ML, et al. Results from prototype II of the BNL simultaneous PET-MRI dedicated breast scanner. IEEE Nuclear Science Symposium Conference Record 2009; 3315–3317.

39. Pichler BJ, Kolb A, Nägele T, Schlemmer HP. PET/MRI: paving the way for the next generation of clinical multimodality imaging applications. J Nucl Med 2010;51(3):333–336.

40. Kang J, Choi Y, Hong KJ, et al. A feasibility study of photosensor charge signal transmission to preamplifier using long cable for development of hybrid PET-MRI. Med Phys 2010;37(11):5655–5664.

41. Wu Y, Catana C, Farrell R, et al. PET performance evaluation of an MR-compatible PET insert. IEEE Trans Nucl Sci 2009;56(3):574–580.

42. Schlemmer HP, Pichler BJ, Schmand M, et al. Simultaneous MR/PET imaging of the human brain: feasibility study. Radiology 2008;248(3):1028–1035.

43. Wehrl HF, Judenhofer MS, Thielscher A, Martirosian P, Schick F, Pichler BJ. Assessment of MR compatibility of a PET insert developed for simultaneous multiparametric PET/MR imaging on an animal system operating at 7 T. Magn Reson Med 2011;65(1):269–279.

44. Wehrl HF, Judenhofer MS, Wiehr S, Pichler BJ. Pre-clinical PET/MR: technological advances and new perspectives in biomedical research. Eur J Nucl Med Mol Imaging 2009;36(Suppl 1):S56–S68.

45. Fontaine R, Belanger F, Viscogliosi N, et al. The hardware and signal processing architecture of LabPET, a small animal APD-based digital PET scanner. IEEE Trans Nucl Sci 2009;56(1):3–9.

46. Drzezga A, Souvatzoglou M, Eiber M, et al. First clinical experience with integrated whole-body PET/MR: comparison to PET/CT in patients with oncologic diagnoses. J Nucl Med 2012;53(6):845–855.

47. Otte AN, Barral J, Dolgoshein B, et al. A test of silicon photomultipliers as readout for PET. Nucl Instr Meth A. 2005;545(3):705–715.

48. Buzhan P, Dolgoshein B, Ilyin A, et al. An advanced study of silicon photomultiplier. ICFA Instrum Bull 2001;23:28–42.

49. Herbert DJ, Saveliev V, Belcari N, D'Ascenzo N, Del Guerra A, Golovin A. First results of scintillator readout with silicon photomultiplier. IEEE Trans Nucl Sci 2006;53(1):389–394.

50. Piemonte C, Battiston R, Boscardin M, et al. New results on the characterization of ITC-irst Silicon photomultipliers. IEEE Nuclear Science Symposium Conference Record 2006; 1566–1569.

51. Llosa G, Belcari N, Bisogni MG, et al. Silicon photomultipliers and SiPM matrices as photodetectors in nuclear medicine. IEEE Nuclear Science Symposium Conference Record 2007; 3220–3223.

52. Renker D, Lorenz E. Advances in solid state photon detectors. J Instr. 2009;4(04):P04004.

53. Conti M. Focus on time-of-flight PET: the benefits of improved time resolution. Eur J Nucl Med Mol Imaging 2011;38(6):1147–1157.

54. Hawkes R, Lucas A, Stevick J, et al. Silicon photomultiplier performance tests in magnetic resonance pulsed fields. IEEE Nuclear Science Symposium Conference Record 2007; 3400–3403.

55. Degenhardt C, Prescher G, Frach T, et al. The digital silicon photomultiplier — A novel sensor for the detection of scintillation light. IEEE Nuclear Science Symposium Conference Record (NSS/MIC) 2009; 2383–2386.

56. Frach T, Prescher G, Degenhardt C, de Gruyter R, Schmitz A, Ballizany R. The digital silicon photomultiplier — Principle of operation and intrinsic detector performance. IEEE Nuclear Science Symposium Conference Record (NSS/MIC) 2009; 1959–1965.

57. von Schulthess GK, Burger C. Integrating imaging modalities: what makes sense from a workflow perspective? Eur J Nucl Med Mol Imaging 2010;37(5):980–990.

58. Martinez-Möller A, Eiber M, Nekolla SG, et al. Workflow and scan protocol considerations for integrated whole-body PET/MRI in oncology. J Nucl Med 2012;53(9):1415–1426.

59. Chun SY, Reese TG, Ouyang J, et al. MRI-based nonrigid motion correction in simultaneous PET/MRI. J Nucl Med 2012;53(8):1284–1291.

60. Kwee TC, Basu S, Saboury B, Alavi A, Torigian DA. Functional oncoimaging techniques with potential clinical applications. Front Biosci (Elite Ed) 2012;4:1081–1096.

61. Shamim SA, Torigian DA, Kumar R. PET, PET/CT, and PET/MRI assessment of breast cancer. PET Clin 2008;3(3):381–393.

62. Hustinx R, Torigian DA, Namur G. Complementary assessment of abdominopelvic disorders with PET/CT and MRI. PET Clin 2008;3(3):435–449.

63. Katz S, Ferrara T, Alavi A, Torigian DA. PET, CT, and MRI for assessment of thoracic malignancy: structure meets function. PET Clin 2008;3(3):395–410.

64. Chen K, Blebea J, Laredo JD, Chen W, Alavi A, Torigian DA. Evaluation of musculoskeleta disorders with PET, PET/CT, and PET/MRI. PET Clin 2008;3(3):451–465.

65. Goldberg MF, Chawla S, Alavi A, Torigian DA,Melhem ER. PET and MRI of brain tumors. PET Clin 2008;3(3):293–315.

66. Antoch G, Bockisch A. Combined PET/MRI: a new dimension in whole-body oncology imaging? Eur J Nucl Med Mol Imaging 2009;36(Suppl 1):S113–S120.

67. Nakajo K, Tatsumi M, Inoue A, et al. Diagnostic performance of fluorodeoxyglucose positron emission tomography/magnetic

resonance imaging fusion images of gynecological malignant tumors: comparison with positron emission tomography/computed tomography. Jpn J Radiol 2010; 28(2):95–100.

68. Torigian DA, Huang SS, Houseni M, Alavi A.Functional imaging of cancer with emphasis on molecular techniques. CA Cancer J Clin 2007;57(4):206–224.
69. Kwee TC, Basu S, Torigian DA, Saboury B, Alavi A. Defining the role of modern imaging techniques in assessing lymph nodes for metastasis in cancer: evolving contribution of PET in this setting. Eur J Nucl Med Mol Imaging 2011;38(7):1353–1366.
70. Boss A, Stegger L, Bisdas S, et al. Feasibility of simultaneous PET/MR imaging in the head and upper neck area. Eur Radiol 2011;21(7):1439–1446.
71. Huang SH, Chien CY, Lin WC, et al. A comparative study of fused FDG PET/MRI, PET/CT, MRI, and CT imaging for assessing surrounding tissue invasion of advanced buccal squamous cell carcinoma. Clin Nucl Med 2011;36(7):518–525.
72. Nagarajah J, Jentzen W, Hartung V, et al. Diagnosis and dosimetry in differentiated thyroid carcinoma using 124I PET: comparison of PET/MRI vs PET/CT of the neck. Eur J Nucl Med Mol Imaging 2011;38(10): 1862–1868.
73. Tatsumi M, Isohashi K, Onishi H, et al. 18F-FDG PET/MRI fusion in characterizing pancreatic tumors: comparison to PET/CT. Int J Clin Oncol 2011;16(4):408–415.
74. Kim SK, Choi HJ, Park SY, et al. Additional value of MR/PET fusion compared with PET/CT in the detection of lymph node metastases in cervical cancer patients. Eur J Cancer 2009;45(12):2103–2109.
75. Donati OF, Hany TF, Reiner CS, et al. Value of retrospective fusion of PET and MR images in detection of hepatic metastases: comparison with 18F-FDG PET/CT and Gd-EOB-DTPA-enhanced MRI. J Nucl Med 2010;51(5):692–699.
76. Antoch G, Vogt FM, Freudenberg LS, et al. Whole-body dual-modality PET/CT and whole-body MRI for tumor staging in oncology. JAMA 2003;290(24):3199–3206.
77. Torigian DA, Lopez RF, Alapati S, et al. Feasibility and performance of novel software to quantify metabolically active volumes and 3D partial volume corrected SUV and metabolic volumetric products of spinal bone marrow metastases on 18F-FDG-PET/CT. Hell J Nucl Med 2011;14(1):8–14.
78. Kwee TC, Basu S, Saboury B, Ambrosini V, Torigian DA, Alavi A. A new dimension of FDG-PET interpretation: assessment of tumor biology. Eur J Nucl Med Mol Imaging 2011;38(6):1158–1170.
79. Kwee TC, Takahara T, Ochiai R, et al. Whole-body diffusion-weighted magnetic resonance imaging. Eur J Radiol 2009; 70(3):409–417.
80. Yong TW, Yuan ZZ, Jun Z, Lin Z, He WZ, Juanqi Z. Sensitivity of PET/MR images in liver metastases from colorectal carcinoma. Hell J Nucl Med 2011;14(3):264–268.
81. Low RN, Gurney J. Diffusion-weighted MRI (DWI) in the oncology patient: value of breathhold DWI compared to unenhanced and gadolinium-enhanced MRI. J Magn Reson Imaging 2007;25(4):848–858.
82. Tan CH, Wang J, Kundra V. Diffusion weighted imaging in prostate cancer. Eur Radiol 2011;21(3):593–603.
83. Laurent V, Trausch G, Bruot O, Olivier P, Felblinger J, Régent D. Comparative study of two whole-body imaging techniques in the case of melanoma metastases: advantages of multi-contrast MRI examination including a diffusion-weighted sequence in comparison with PET-CT. Eur J Radiol 2010;75(3):376–383.
84. Kim YN, Yi CA, Lee KS, et al. A proposal for combined MRI and PET/CT interpretation criteria for preoperative nodal staging in non-small-cell lung cancer. Eur Radiol 2012;22(7):1537–1546.
85. Park SH, Moon WK, Cho N, et al. Comparison of diffusion-weighted MR imaging and FDG PET/CT to predict pathological complete response to neoadjuvant chemotherapy in patients with breast cancer. Eur Radiol 2012;22(1):18–25.
86. Park H, Wood D, Hussain H, et al. Introducing parametric fusion PET/MRI of primary prostate cancer. J Nucl Med 2012; 53(4):546–551.
87. Wolf W. The unique potential for noninvasive imaging in modernizing drug development and in transforming therapeutics: PET/MRI/MRS. Pharm Res 2011;28(3):490–493.
88. Benveniste H, Fowler JS, Rooney WD, et al. Maternal-fetal in vivo imaging: a combined PET and MRI study. J Nucl Med 2003;44(9):1522–1530.
89. Alessio AM, Kinahan PE. CT protocol selection in PET-CT imaging. http://www.imagewisely.org/Imaging-Professionals/Nuclear-Medicine/Articles/CT-Protocol-Selection. 2012:1–4.
90. Akin EA, Torigian DA. Considerations regarding radiation exposure in performing FDG-PET-CT. http://www.imagewisely.org/Imaging-Professionals/Nuclear-Medicine/Articles/Considerations. 2012:1–7.
91. Musiek ES, Torigian DA, Newberg AB. Investigation of non-neoplastic neurologic disorders with PET and MRI. PET Clin 2008;3(3):317–334.
92. Heiss WD. The potential of PET/MR for brain imaging. Eur J Nucl Med Mol Imaging 2009;36(Suppl 1):S105–S112.
93. Schlemmer HP, Pichler BJ, Krieg R, Heiss WD. An integrated MR/PET system: prospective applications. Abdom Imaging 2009; 34(6):668–674.
94. Boss A, Bisdas S, Kolb A, et al. Hybrid PET/MRI of intracranial masses: initial experiences and comparison to PET/CT. J Nucl Med 2010;51(8):1198–1205.
95. Cho ZH, Son YD, Kim HK, et al. Substructural hippocampal glucose metabolism observed on PET/MRI. J Nucl Med 2010; 51(10):1545–1548.
96. Basu S, Zaidi H, Houseni M, et al. Novel quantitative techniques for assessing regional and global function and structure based on modern imaging modalities: implications for normal variation, aging and diseased states. Semin Nucl Med 2007; 37(3):223–239.
97. Alavi A, Newberg AB, Souder E, Berlin JA. Quantitative analysis of PET and MRI data in normal aging and Alzheimer's disease: atrophy weighted total brain metabolism and absolute whole brain metabolism as reliable discriminators. J Nucl Med 1993; 34(10):1681–1687.
98. Schwenzer NF, Stegger L, Bisdas S, et al. Simultaneous PET/MR imaging in a human brain PET/MR system in 50 patients—current state of image quality. Eur J Radiol 2012;81(11):3472–3478.
99. Cho ZH, Son YD, Kim HK, et al. Observation of glucose metabolism in the thalamic nuclei by fusion PET/MRI. J Nucl Med 2011;52(3):401–404.
100. Son YD, Cho ZH, Kim HK, et al. Glucose metabolism of the midline nuclei raphe in the brainstem observed by PET-MRI fusion imaging. Neuroimage 2012;59(2):1094–1097.
101. Naidich TP, Duvernoy HM, Delman BN, Sorensen AG, Kollias SS, Haacke EM. Duvernoy's atlas of the human brain stem and cerebellum. High-field MRI: surface anatomy, internal structure, vascularization and 3D sectional anatomy. Vienna, Austria: Springer-Verlag, 2009.
102. Eggers C, Szelies B, Bauer B, et al. Imaging ofacetylcholine esterase activity in brainstem nuclei involved in regulation of sleep and wakefulness. Eur J Neurol 2007; 14(6):690–693.
103. Lee KK, Salamon N. [18F] fluorodeoxyglucose-positron-emission tomography and MR imaging coregistration for presurgical evaluation of medically refractory epilepsy. AJNR Am J Neuroradiol 2009; 30(10):1811–1816.

104. Salamon N, Kung J, Shaw SJ, et al. FDG-PET/MRI coregistration improves detection of cortical dysplasia in patients with epilepsy. Neurology 2008;71(20):1594–1601.

105. Cruz LC Jr, Sorensen AG. Diffusion tensor magnetic resonance imaging of brain tumors. Magn Reson Imaging Clin N Am 2006;14(2):183–202.

106. Boss A, Kolb A, Hofmann M, et al. Diffusion tensor imaging in a human PET/MR hybrid system. Invest Radiol 2010; 45(5):270–274.

107. Vlieger EJ, Majoie CB, Leenstra S, Den Heeten GJ. Functional magnetic resonance imaging for neurosurgical planning in neurooncology. Eur Radiol 2004;14(7): 1143–1153.

108. Ogawa S, Lee TM, Kay AR, Tank DW. Brain magnetic resonance imaging with contrast dependent on blood oxygenation. Proc Natl Acad Sci U S A 1990;87(24):9868–9872.

109. Behera D, Jacobs KE, Behera S, Rosenberg J,Biswal S. (18)F-FDG PET/MRI can be used to identify injured peripheral nerves in a model of neuropathic pain. J Nucl Med 2011;52(8):1308–1312.

110. Takalkar A, Chen W, Desjardins B, Alavi A, Torigian DA. Cardiovascular imaging with PET, CT, and MRI. PET Clin 2008; 3(3):411–434.

111. Bengel FM, Ueberfuhr P, Schiepel N, Nekolla SG, Reichart B, Schwaiger M. Myocardial efficiency and sympathetic reinnervation after orthotopic heart transplantation: a noninvasive study with positron emission tomography. Circulation 2001; 103(14):1881–1886.

112. Syed IS, Feng D, Harris SR, et al. MR imaging of cardiac masses. Magn Reson Imaging Clin N Am 2008;16(2):137–164, vii.

113. Probst S, Seltzer A, Spieler B, Chachoua A, Friedman K. The appearance of cardiac metastasis from squamous cell carcinoma of the lung on F-18 FDG PET/CT and post hoc PET/MRI. Clin Nucl Med 2011;36(4): 311–312.

114. Higuchi T, Anton M, Dumler K, et al. Combined reporter gene PET and iron oxide MRI for monitoring survival and localization of transplanted cells in the rat heart. J Nucl Med 2009;50(7):1088–1094.

115. Bural GG, Torigian DA, Chamroonrat W, et al. Quantitative assessment of the atherosclerotic burden of the aorta by combined FDG-PET and CT image analysis: a new concept. Nucl Med Biol 2006;33(8):1037–1043.

116. Tahara N, Kai H, Ishibashi M, et al. Simvastatin attenuates plaque inflammation: evaluation by fluorodeoxyglucose positron emission tomography. J Am Coll Cardiol 2006;48(9):1825–1831.

117. Fayad ZA, Mani V, Woodward M, et al. Safety and efficacy of dalcetrapib on atherosclerotic disease using novel non-invasive multimodality imaging (dal-PLAQUE): a randomised clinical trial. Lancet 2011; 378(9802):1547–1559.

118. Basu S, Chryssikos T, Houseni M, et al. Potential role of FDG PET in the setting of diabetic neuro-osteoarthropathy: can it differentiate uncomplicated Charcot's neuroarthropathy from osteomyelitis and soft-tissue infection? Nucl Med Commun 2007; 28(6):465–472.

119. Nawaz A, Torigian DA, Siegelman ES, Basu S,Chryssikos T, Alavi A. Diagnostic performance of FDG-PET, MRI, and plain film radiography (PFR) for the diagnosis of osteomyelitis in the diabetic foot. Mol Imaging Biol 2010;12(3):335–342.

120. Beckers C, Jeukens X, Ribbens C, et al. (18)F-FDG PET imaging of rheumatoid knee synovitis correlates with dynamic magnetic resonance and sonographic assessments as well as with the serum level of metalloproteinase-3. Eur J Nucl Med Mol Imaging 2006;33(3):275–280.

121. El-Haddad G, Kumar R, Pamplona R, Alavi A. PET/MRI depicts the exact location of meniscal tear associated with synovitis. Eur J Nucl Med Mol Imaging 2006;33(4): 507–508.

122. Blebea JS, Houseni M, Torigian DA, et al. Structural and functional imaging of normal bone marrow and evaluation of its age-related changes. Semin Nucl Med 2007;37(3): 185–194.

123. Miese F, Scherer A, Ostendorf B, et al. Hybrid 18F-FDG PET-MRI of the hand in rheumatoid arthritis: initial results. Clin Rheumatol 2011;30(9):1247–1250.

124. Tanna NK, Kohn MI, Horwich DN, et al. Analysis of brain and cerebrospinal fluid volumes with MR imaging: impact on PET data correction for atrophy. Part II. Aging and Alzheimer dementia. Radiology 1991; 178(1):123–130.

125. Bural GG, Torigian DA, Burke A, et al. Quantitative assessment of the hepatic metabolic volume product in patients with diffuse hepatic steatosis and normal controls through use of FDG-PET and MR imaging: a novel concept. Mol Imaging Biol 2010;12(3):233–239.

126. Basu S, Houseni M, Bural G, et al. Magnetic resonance imaging based bone marrow segmentation for quantitative calculation of pure red marrow metabolism using 2-deoxy-2-[F-18]fluoro-D-glucose-positron emission tomography: a novel application with significant implications for combined structure-function approach. Mol Imaging Biol 2007;9(6):361–365.

127. Nawaz A, Torigian D, Zhuang H, Alavi A. Study on the correlation of atherosclerosis in the popliteal artery with metabolic activity and metabolic volumetric product of the diabetic foot. J Nucl Med 2008;49(Suppl 1):197P.

128. von Schulthess GK, Schlemmer HP. A look ahead: PET/MR versus PET/CT. Eur J Nucl Med Mol Imaging 2009;36(Suppl 1):S3–S9.

129. Brix G, Nekolla EA, Nosske D, Griebel J. Risks and safety aspects related to PET/MR examinations. Eur J Nucl Med Mol Imaging 2009;36(Suppl 1):S131–S138.

130. Koyama S, Nakahara T, Sakurai T, Komatsubara Y, Isozumi Y, Miyakoshi J. Combined exposure of ELF magnetic fields and x-rays increased mutant yields compared with x-rays alone in pTN89 plasmids. J Radiat Res (Tokyo) 2005;46(2):257–264.

131. Miyakoshi J, Yoshida M, Shibuya K, Hiraoka M. Exposure to strong magnetic fields at power frequency potentiates X-ray-induced DNA strand breaks. J Radiat Res (Tokyo) 2000;41(3):293–302.

132. Walleczek J, Shiu EC, Hahn GM. Increase in radiation-induced HPRT gene mutation frequency after nonthermal exposure to nonionizing 60 Hz electromagnetic fields. Radiat Res 1999;151(4):489–497.

133. Hintenlang DE. Synergistic effects of ionizing radiation and 60 Hz magnetic fields. Bioelectromagnetics 1993;14(6):545–551.

134. Miyakoshi J. Effects of static magnetic fields at the cellular level. Prog Biophys Mol Biol 2005;87(2-3):213–223.

135. Theysohn JM, Maderwald S, Kraff O, Moenninghoff C, Ladd ME, Ladd SC. Subjective acceptance of 7 Tesla MRI for human imaging. MAGMA 2008;21(1-2):63–72.

136. Cho ZH, Son YD, Choi EJ, et al. In-vivo human brain molecular imaging with a brain-dedicated PET/MRI system. MAGMA 2013;26(1):71–79.